A Numerical Investigation of a Convectively Generated, Inertially Stable, Extratropical Warm-Core Mesovortex over Land. Part I: Structure and Evolution

DA-LIN ZHANG

National Center for Atmospheric Research, Boulder, Colorado*

J. MICHAEL FRITSCH

Department of Meteorology, The Pennsylvania State University, University Park, Pennsylvania

(Manuscript received 11 April 1988, in final form 28 June 1988)

ABSTRACT

A 36-h nested-grid numerical simulation of the life cycle of a convectively generated, inertially stable, warm-core mesovortex is presented. The vortex evolved from a mesoscale convective complex that developed from a squall line over Oklahoma during 7–8 July 1982. A modified version of the Pennsylvania State University/National Center for Atmospheric Research mesoscale hydrostatic model with a fine-mesh grid resolution of 25 km is utilized for this study. The model simultaneously incorporates parameterized convection and a grid-resolved convective scheme containing the effects of hydrostatic water loading, condensation (evaporation), freezing (melting) and sublimation.

Genesis, intensification and maintenance of a low- to midtropospheric closed meso-β scale cyclone as well as the associated surface pressure perturbations, the evolution of moist convection, and the distribution and magnitude of total rainfall are simulated by the model. Similarly, the observed amplification of a 700-mb meso-α scale short-wave trough, the development of a midlevel warm-core structure and an upper-level mesoanticyclone during the mature stage, the quasi-stationary nature of the vortex circulation, and the vertical distribution of horizontal wind and relative vorticity in the vicinity of the rotating mesoscale convective system (MCS) are all reasonably well simulated up to 36 h. During the mature stage of the rotating MCS, both the observed and simulated vertical structures are characterized by a low-level mesohigh in association with a cool pool and sinking motion, a midtropospheric warm-core structure, and an upper-level cold dome with an associated anticyclonic circulation. The horizontal momentum and equivalent potential temperature are uniformly distributed in the vortex layer with the vorticity maximum located between 600 and 700 mb.

The model simulation shows that the upward motion and cyclonic vorticity associated with the front and vortex system are out of phase. The phase difference appears to be a propagation mechanism of the rotating MCS and the low-level front. Another important finding is that most of the vortex properties tilt downstream with height during the decay period. Such a vertical distribution helps explain why a well-defined and long-lived hydrostatic *surface* mesolow did not form in either the observations or the simulation. It also helps explain why other midlatitude rotating MCSs often exhibit weak surface pressure perturbations.

It is found that a propagating mesoscale vorticity disturbance, preexisting low-level frontal forcing and a convectively favorable environment ahead of the front help generate an organized area of upward motion wherein the vortex develops. However, it is the resolvable-scale latent heat release that appears to be directly responsible for producing the rotating MCS. The quasi-stationary nature of the rotating MCS is related to the fact that the vortex develops within a slow-moving, low-level horizontal deformation field. The vortex is well maintained because of the weak horizontal and vertical shear in the deformation zone and the generated large inertial stability of the vortex. The results indicate that in some situations, numerical forecasts of the genesis, evolution and rainfall of rotating MCSs are possible up to 36 h using the currently available observations if a high-grid resolution model can be utilized.

1. Introduction

One of the most exciting recent discoveries in mesometeorology is that some mesoscale convective systems (MCSs) develop a warm-core vortical circulation within their stratiform region (Houze 1977; Ogura and Liou 1980; Smull and Houze 1985; Leary and Rappaport 1987). Hereafter, these weather systems are referred to as *rotating MCSs*. These rotating cloud systems can become inertially stable and sometimes persist for several days until their vorticity is absorbed by the larger-scale flow (Johnston 1981; Wetzel et al. 1983; Kuo et al. 1986; Menard et al. 1986). In some cases, the inertially stable vortices appear to be responsible for multiple MCS development (Johnston 1981), and,

* The National Center for Atmospheric Research (NCAR) is funded by the National Science Foundation.

Corresponding author address: Dr. Da-Lin Zhang, Department of Physics, University of Toronto, Toronto, Ontario, Canada M55 1A7.

in the appropriate larger-scale environment, are observed to be a precursor to tropical cyclogenesis (Velasco and Fritsch 1987). There is increasing observational evidence that the rotating MCSs are closely associated with a particular type of MCSs, termed by Maddox (1980) the mesoscale convective complex (MCC; see Johnston 1981; Johnson 1986; Velasco and Fritsch 1987). In particular, the characteristic circular cold cloud shields of MCCs suggest that the mesovortices may be their primary organizational feature. Another particularly important aspect of rotating MCSs is that stratiform precipitation seems to play a significant role in the amplification of the vortex circulation (see Houze 1977; Churchill and Houze 1984; Leary and Rappaport 1987; and discussions in Zhang and Fritsch 1987, 1988). These interesting findings have been confirmed by a number of observational studies from different geographic locations, for example, in the United States (Johnston 1981; Johnson 1986; Smull and Houze 1987), China (called "southwest vortex" by Chinese meteorologists) (Chen and Dell'Osso 1984; Wu and Chen 1985; Kuo et al. 1986; Wang and Orlanski 1987), and South America (Velasco and Fritsch 1987).

Recently, increasing attention has been paid to investigating the cause and effect of mesovortices with respect to the development, structure and persistence of MCCs or rotating MCSs. However, the thorough understanding of the processes which initiate and maintain the vortex circulation poses a particular challenge to atmospheric scientists. For instance, as is well known, the accurate prediction of the development and propagation of rotating MCSs and associated precipitation is not readily achieved by numerical models nor subjective techniques since most of these systems are not well resolved by the current observational network. Moreover, they are basically barotropic in nature and often form within an environment in which the larger-scale dynamic forcing (e.g., vorticity advection, thermal advection, and/or frontal lifting) is weak. This issue has been recognized as part of the reason why the warm-season quantitative precipitation forecasts (QPFs) lag significantly behind the cold-season QPFs (Ramage 1982; Georgakakos and Hudlow 1984; Heideman and Fritsch 1988). Furthermore, the attendent strong mesoscale circulation and inertial stability of rotating MCSs sometimes induce redevelopment of deep convection and produce heavy stratiform precipitation or flash floods (Bosart and Sanders 1981; Kuo et al. 1986) even long after the intense convection that spawned them has ceased. Thus, rotating MCSs also pose a particular threat to human safety and economic well-being. There is widespead agreement that progress in improving our knowledge of rotating MCSs is mainly limited by observations which are too coarse in both time and space to resolve basic features of MCSs. In fact, a recently conducted PRE-STORM experiment with an improved resolution observational network has revealed several vortex events in association with MCCs and provided much new information on the detailed structure and evolution of rotating MCSs (Johnson 1986; Brandes 1987; Augustine and Howard 1987). Alternatively, the usual lack of high-resolution observations has made numerical models a very important tool for investigating the dynamics, structure and evolution of rotating MCSs and associated upscale (downscale) interaction with the larger-scale environment (deep convection).

Therefore, in view of the above consideration, numerical investigation of rotating MCSs is of more than scientific interest. In particular, since the inertial stability associated with the rotating MCSs can lengthen the lifetime of those weather systems (see Smith 1981; Schubert and Hack 1982; Zhang and Fritsch 1987), it should make them more deterministic in terms of numerical prediction of their evolution, and interaction with their environment. This possibility forms one of the hypotheses for the present study. That is, if numerical models could predict the occurrence of the mesovortex at the right time and location, it should be possible to forecast the vortex path and the distribution of rainfall as well. This might be an important issue for the improvement of warm-season QPFs since Fritsch et al. (1986) estimated that more than half of the central United States precipitation during the growing season is produced by MCCs (i.e., rotating MCSs).

The purpose of this paper is to present a 36-h nested-grid simulation involving the life cycle of an Oklahoma *meso-β scale rotating MCS* during 0000 UTC 7 July–1200 UTC 8 July 1982 *using the standard upper-air observations.* Hence, this study also attempts to test the additional hypothesis that certain large-scale environments contain a sufficiently well-defined signal (e.g., from frontal forcing, or vorticity or thermal advection) such that meso-β scale features can be properly generated in a high-resolution model by nonlinear wave–wave interaction. The rotating MCS initiated from a squall line that formed during early evening of 7 July. The squall line developed along and ahead of a shallow low-level frontal system, and, during the nighttime hours, transformed into an MCC with an upper-tropospheric anticyclonic outflow clearly visible in the satellite imagery. The intense MCC resulted in locally heavy rainfall with a 12-h maximum value exceeding 100 mm. A rotating cloud system produced by this MCC persisted for more than 36 hours. The operational Limited-area Fine-mesh Model (LFM) failed to predict the genesis and subsequent evolution of the mesovortex, and associated rainfall magnitude and path for this case. Section 2 describes the basic model physics used for this study. Section 3 shows data sources and initial conditions. In section 4, the model simulation is compared with observations. After some confidence in the model simulation is established, some nonobservable details of the structure and evolution

of the rotating MCS are described. Summary and concluding remarks are given in the last section.

2. Model description

The model used for this case study is an improved version of the Pennsylvania State University/National Center for Atmospheric Research (PSU/NCAR) mesoscale hydrostatic model described by Anthes et al. (1987); it is very similar to the version used by Zhang and Fritsch (1986a), Zhang et al. (1988), and Zhang (1989) for the case study of the 1977 Johnstown flood events. The following model features are considered to be very important for the numerical simulation of the lifecycle of a rotating MCS:

- an explicit convective scheme containing predictive equations for cloud water (ice) and rainwater (snow), which follows Hsie et al. (1984), Lin et al. (1983) and Rutledge and Hobbs (1983), as described by Zhang (1989);
- a two-way interactive nested-grid procedure (Zhang et al. 1986);
- an improved implicit convective scheme of Fritsch–Chappell (1980; Zhang and Fritsch 1986a) for the fine mesh and Anthes–Kuo (Anthes and Keyser 1979) for the coarse mesh portion of the nested-grid model; and
- a modified version of the Blackadar "large-eddy exchange" planetary boundary layer (PBL) parameterization (Zhang and Anthes 1982; Zhang and Fritsch 1986a).

The nested-grid ratio is 1 to 3 with a fine-mesh length of 25 km and a coarse-mesh length of 75 km. The (x, y, σ) dimensions of the coarse and fine meshes are 45 $\times$ 37 $\times$ 19 and 67 $\times$ 49 $\times$ 19, respectively. The vertical coordinate, σ, is defined as $\sigma = (p - p_t)/(p_s - p_t)$ where p_t and p_s are the pressures at the top and the surface of the model, respectively. The value of p_t is 80 mb in this case. The 19 computational σ layers are 0.9985, 0.977, 0.929, 0.873, 0.817, 0.761, 0.7045, 0.6475, 0.5705, 0.535, 0.4705, 0.41, 0.3505, 0.272, 0.2345, 0.178, 0.125, 0.075, 0.025, which are the same as that used by Zhang and Fritsch (1986a). Figure 1 shows the model domain of both fine and coarse meshes, and the terrain distribution used for this study. Although the western nested interface is laid near the highest terrain of the Rocky Mountains in Colorado, no important noise was noted in the 36-h model simulation. Zhang et al. (1986) showed another example of a numerically smooth solution when the interface was located near the highest terrain of the Rocky Mountains. In order to show more details of the simulated rotating MCS, a subarea of the fine-mesh domain (see Fig. 1) will be utilized in the discussion of the fine-mesh model results.

It should be noted that the implicit and explicit schemes are operating simultaneously in the model to

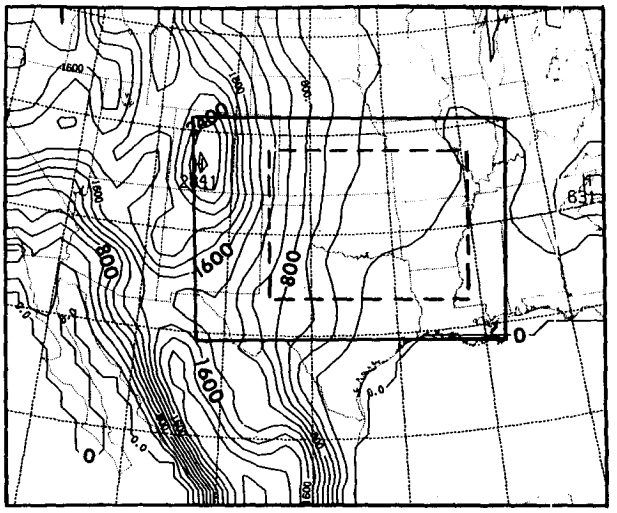

FIG. 1. The nested-grid domain and terrain distribution (m). The interior thick solid lines denote the mesh interface and the dashed lines indicate the subdomain used for the presentation of the fine-mesh simulation.

account for the separate effects of subgrid-scale convective forcing and resolvable-scale phase changes. For the convenience of model description, the explicit convective scheme computes "stratiform" or resolvable-scale precipitation which is generated within a saturated atmosphere (i.e., 100% relative humidity), whereas the implicit convective schemes obtain parameterized convective precipitation which forms in a conditionally unstable and favorably forced but not necessarily saturated environment. Zhang et al. (1988) showed that even with a grid resolution of 12.5 km, an implicit convective scheme is still essential for reproducing MCSs under a conditionally unstable environment. They also showed that the simultaneous incorporation of implicit and explicit convective schemes (termed the full physics approach) does not double account for either resolvable-scale or parameterized heating and moistening, and appears to be the best approach to handling both the convective and stratiform precipitation.

The explicit convective scheme contains the effects of hydrostatic water loading, condensation and evaporation, freezing and melting, and deposition/sublimation processes. These resolvable-scale model physics have been found to be essential for reproducing reasonable magnitudes of mesoscale circulations and surface pressure perturbations (see Molinari and Dudek 1986; Zhang et al. 1988), and also for controlling the unrealistic development of conditional instability of the second kind (or a CISK-like instability). The CISK-like instability is referred to by Zhang et al. (1988) as an overenhanced positive feedback process among latent heat release, moisture convergence and the surface pressure fall. Addition of freezing and melting effects

further helps the model simulation conform to the observations and retard the development of the CISK-like instability (see Zhang 1989).

The implicit Fritsch–Chappell convective scheme and the PBL parameterization are basically identical to that used by Zhang and Fritsch (1986a). For simplicity of the model development, the geographic distribution of surface parameters (e.g., moisture availability, roughness length, albedo and thermal capacity) which determine surface energy budgets and the development of the PBL, is designed to be similar to that employed by Benjamin and Carlson (1986). The time-dependent coarse-mesh lateral boundary conditions are obtained by interpolating the 12 h observational analyses linearly in time and then specifying them according to Perkey and Kreitzberg (1976). For a more detailed description of the different model aspects, the reader is referred to Zhang and Fritsch (1986a), Anthes et al. (1987), and Zhang (1989).

3. Initialization and initial conditions

a. Initialization

According to the observational analysis of Menard et al. (1986), the model should be initialized at 0000 UTC 7 July 1982. Unfortunately, the National Meteorological Center (NMC) global analysis for that 2-week period is not available for preprocessing model initial conditions as a first guess. The only obtainable global analysis is the daily 1200 UTC analysis by the European Centre for Medium-range Weather Forecasts (ECMWF) which is archived at NCAR. It is well known that the first-guess fields play an important role in determining the quality of initial conditions and the subsequent model simulation. In order to properly create the first-guess fields of temperature, relative humidity, horizontal winds and surface pressure for 0000 UTC 7 July, a 12-h model forecast with a much larger domain size needed to be made using the available 1200 UTC 6 July data. In doing so, the ECMWF 1200 UTC analysis was first interpolated to the coarse-grid mesh with a domain size of 55 × 47 × 19, and then modified by a series of successive scans using standard rawinsonde soundings (see Benjamin and Seaman 1985). Finally, the vertically integrated divergence in a column was removed from the horizontal wind field prior to the 12-h coarse-mesh forecast.

After the first-guess fields were created from the model forecast, the nested-grid model was initialized following Zhang et al. (1986) and Zhang and Fritsch (1986a). Note that no balancing between mass and wind fields is performed in the initialization procedure. It should also be pointed out that there are no artificially constructed upper-air soundings used for preprocessing initial data. However, the reported high-resolution sea-level pressure, surface temperature and moisture have been subjectively analyzed before being incorporated into the model initial conditions, and they were found to be important in helping define the position of a surface frontal system as well as the distribution of the pressure pattern and the moisture gradient.

b. Initial conditions

The prestorm environment at 0000 UTC 7 July is outlined in Figs. 2–5. A weak, shallow cold front extends from northern Texas through Oklahoma into Ontario, Canada. Associated with it, a strong equivalent potential temperature (θ_e) gradient, mostly due to the moisture distribution (i.e., dry line), is superimposed with a lower-level horizontal deformation field over the area where the rotating MCS is to develop (see Fig. 2a). Such a flow and moisture juxtaposition persists

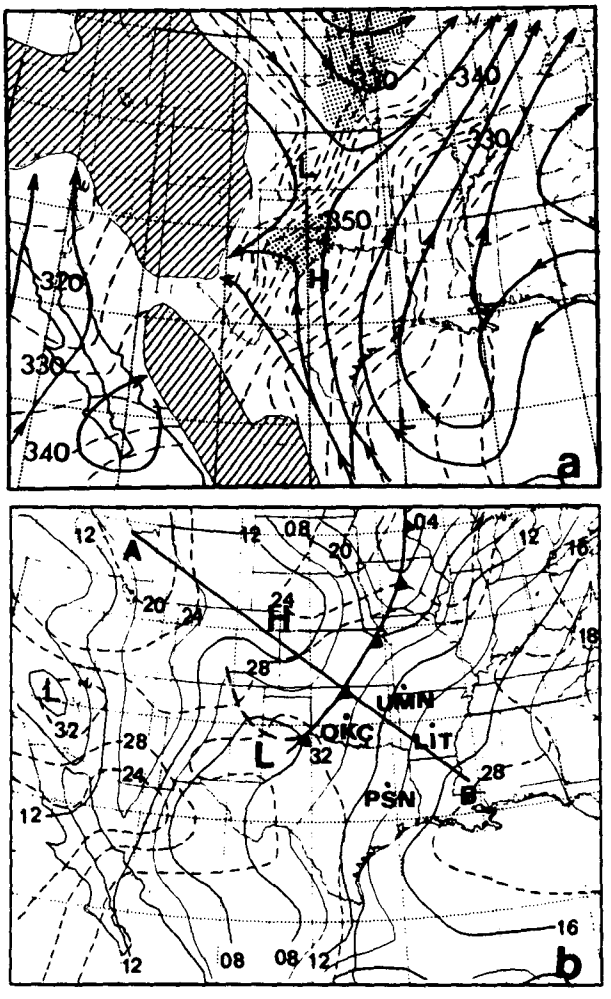

FIG. 2. (a) Analysis of 850 mb streamlines (solid lines) and θ_e (dashed lines at intervals of 5 K) for 0000 UTC 7 July 1982. Cross-hatching indicates the ground above the 850 mb level and shading denotes cyclonic vorticity exceeding 4×10^{-5} s^{-1}. (b) Corresponding surface analysis. Solid lines are isobars (mb) and dashed lines are isotherms (°C). The large dots are locations of rawinsonde observations in the fine-mesh domain.

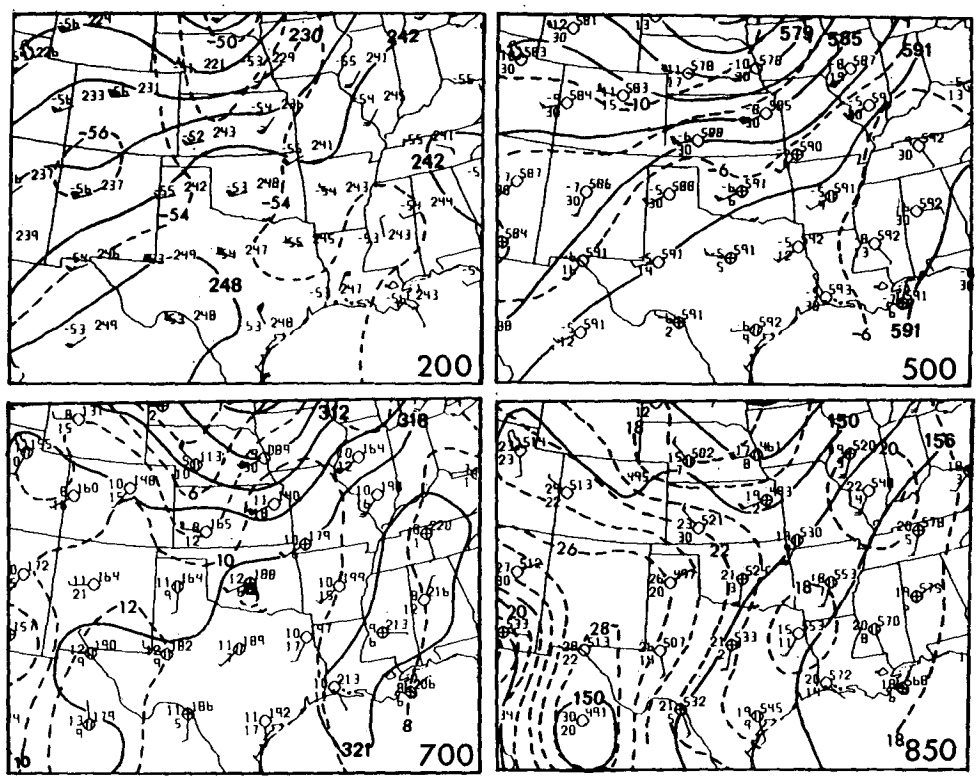

FIG. 3. Upper air analyses of height (solid lines), temperature (dashed lines), dew point and horizontal winds for 0000 UTC 7 July 1982 (adapted from Menard 1988). Wind speed is in m s^{-1} and a full barb is 5 m s^{-1}.

for the subsequent 36 h and is favorable for low-level frontogenesis, especially if *virtual* temperature effects are considered. Because of a large subtropical high situated over the eastern United States, there is a branch of low-level, high-θ_e air from central Texas flowing northward into central Oklahoma ahead of the surface front. The related maximum winds are within the 900–800 mb layer. The resulting moisture convergence, coupled with the weak forcing from a midtropospheric short wave to the north (Fig. 3) has created a column

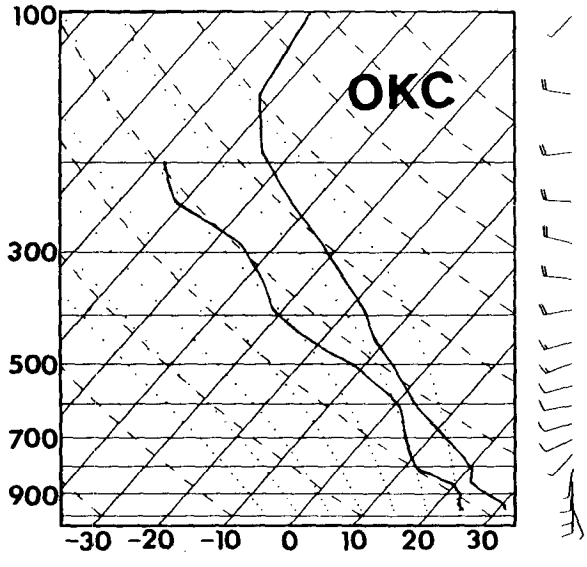

FIG. 4. Observed sounding for OKC, Oklahoma at 0000 UTC 7 July 1982 (See Fig. 2 for the location.) A full barb is 10 m s^{-1}.

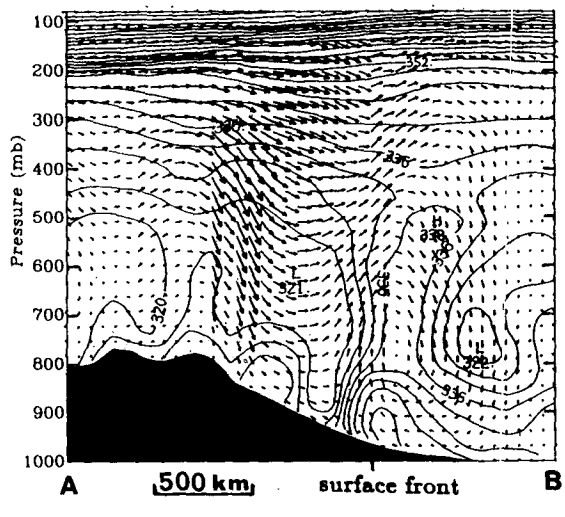

FIG. 5. Cross section of equivalent potential temperature (solid line, K) and vertical circulation vectors along line AB in Fig. 2.

of high-θ_e air over the central Oklahoma region; this column exhibits considerable convective available potential energy (CAPE) (see Figs. 4 and 5). The total totals analysis by Menard et al. (1986) also revealed widespread large amounts of CAPE (total totals $\approx$ 50–60) ahead of the front prior to the MCC genesis. In fact, as shown in Fig. 6, a long line of thunderstorms was already well developed by 2230 UTC 6 July along and ahead of the front. The important role of a mid-tropospheric short wave in helping initiate a vortex circulation has been demonstrated by Zhang and Fritsch (1986b) in the simulation of the 1977 Johnstown flood events. In the present case, however, the existing short-wave forcing is extremely weak at best and does not appear to play a crucial role in the organization of the MCC.

Note the cyclonic distribution of convective clouds over north-central Texas (Fig. 6) which is coincident with a notable cyclonic vorticity center (Fig. 2a) and a 700 mb short wave (Fig. 3) over that region. The northeastward propagation of this cyclonic vorticity appears to assist the generation of the mesovortex,

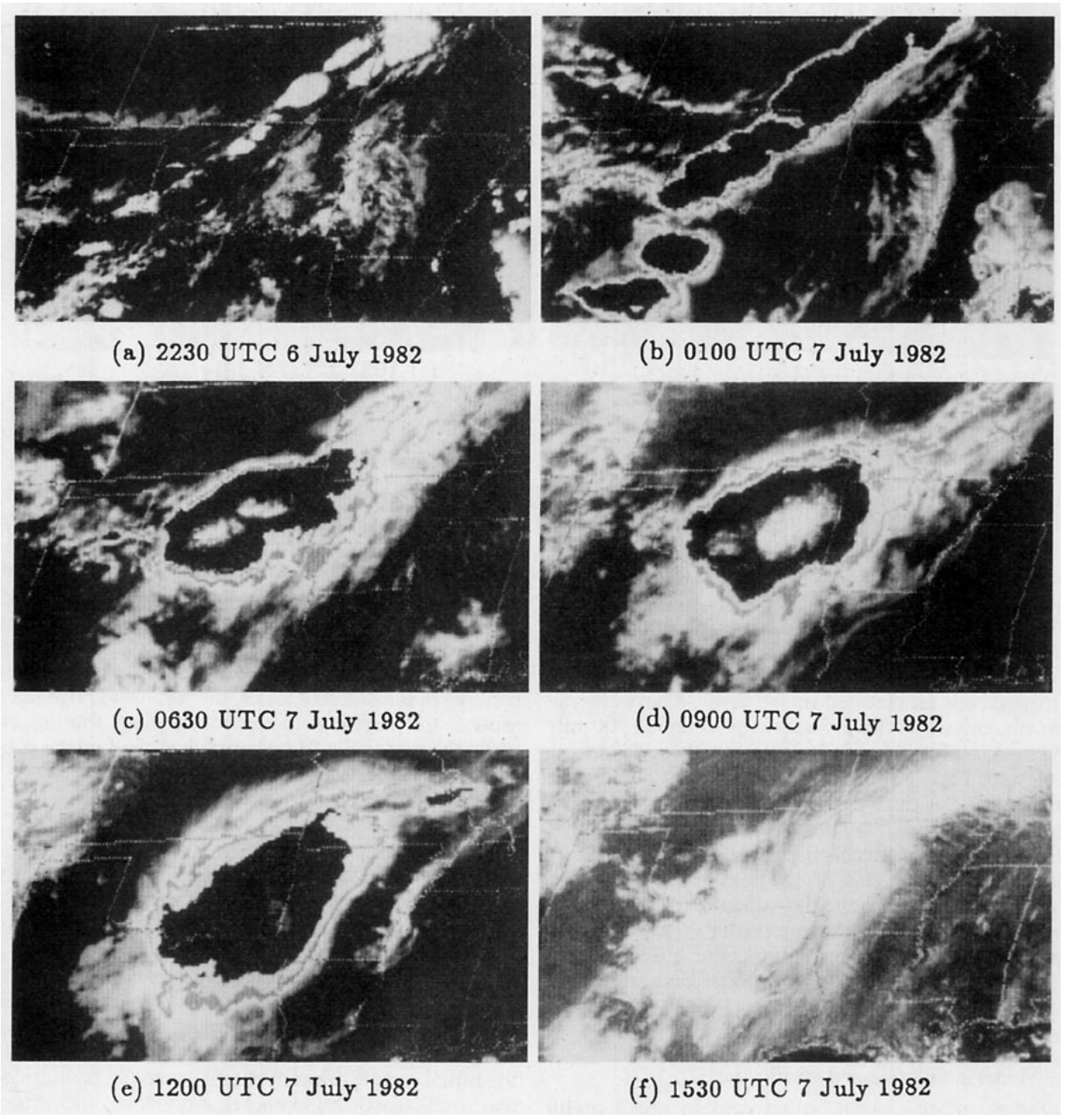

FIG. 6. (a–j). GOES-1 visible and infrared satellite imagery for the times indicated.

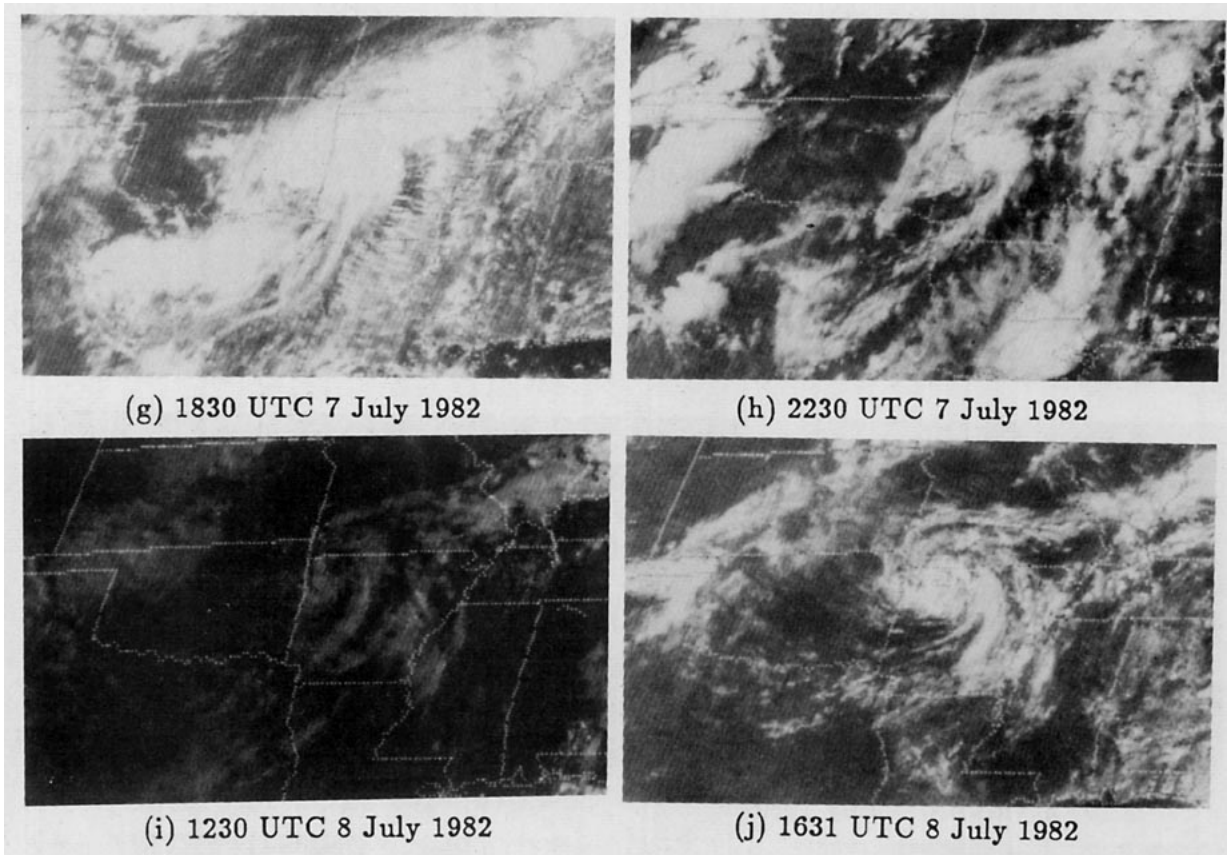

FIG. 6. (*Continued*)

namely, it tends to increase dynamic efficiency of the latent heat release in producing warm-core structure, as discussed by Hack and Schubert (1986). Note also the Oklahoma City (OKC) sounding (Fig. 4) in which there is a high-θ_e layer from the surface to about 850 mb with a weak inversion above. This thermodynamic structure is very similar to the conceptual model proposed by Carlson et al. (1983) in which southerly moist air underruns an elevated mixed layer. Above the inversion, the wind sharply veers up to about 700 mb and then the flow is basically westerly with weak vertical shear (see Figs. 3 and 4). As discussed by Zhang and Fritsch (1987), the weak shearing environment is favorable for the maintenance of vortices once they have formed. Moreover, according to Hoskins et al. (1984) and Cho and Chan (1987), the presence of mesoscale temperature inhomogeneities (at lower levels in this case) is conducive to the mesoscale organization of upward motion and precipitation. For a detailed description of the present observational case study, the reader is referred to Menard et al. (1986) and Menard (1988).

4. Model simulation and verification

Since surface analyses often contain much useful information about the evolution and air flow structure of MCSs, and are also an important measure of a model's performance, section 4a describes verification of the simulated surface features (including rainfall distribution and characteristics) against the mesoanalysis by Menard (1988). Section 4b presents the observed and simulated structure and evolution of the vortex and the surrounding tropospheric flow. In order to clearly show important meteorological events and flow patterns of the different scales, the simulated large-scale aspects are presented in the coarse-mesh framework while the mesoscale features are displayed in the subdomain of the fine-mesh framework.

a. Evolution of surface structures

Inspection of satellite imagery (Fig. 6) and hourly rainfall indicates that the squall line was initiated around 2200 UTC 6 July along the low-level front. Although the model was initialized at 0000 UTC 7 July and the observed squall line was not resolved by the rawinsonde network, the implicit Fritsch–Chappell convective scheme did not have any difficulty in generating model convection at a reasonable place during the initial couple of model hours since the frontal system, particularly the low-level, west–east temperature gradient in combination with the horizontal defor-

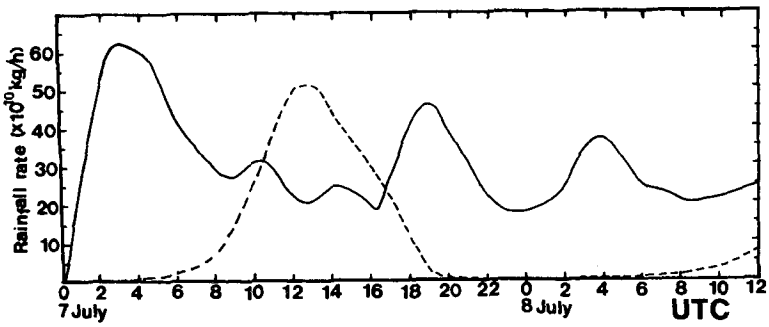

FIG. 7a. The simulated time evolution (0000 UTC 7 July–1200 UTC 8 July) of the rainfall rate (10^{10} kg h^{-1}) in the subdomain. Solid and dashed lines denote implicit and explicit convective rainfall rates, respectively.

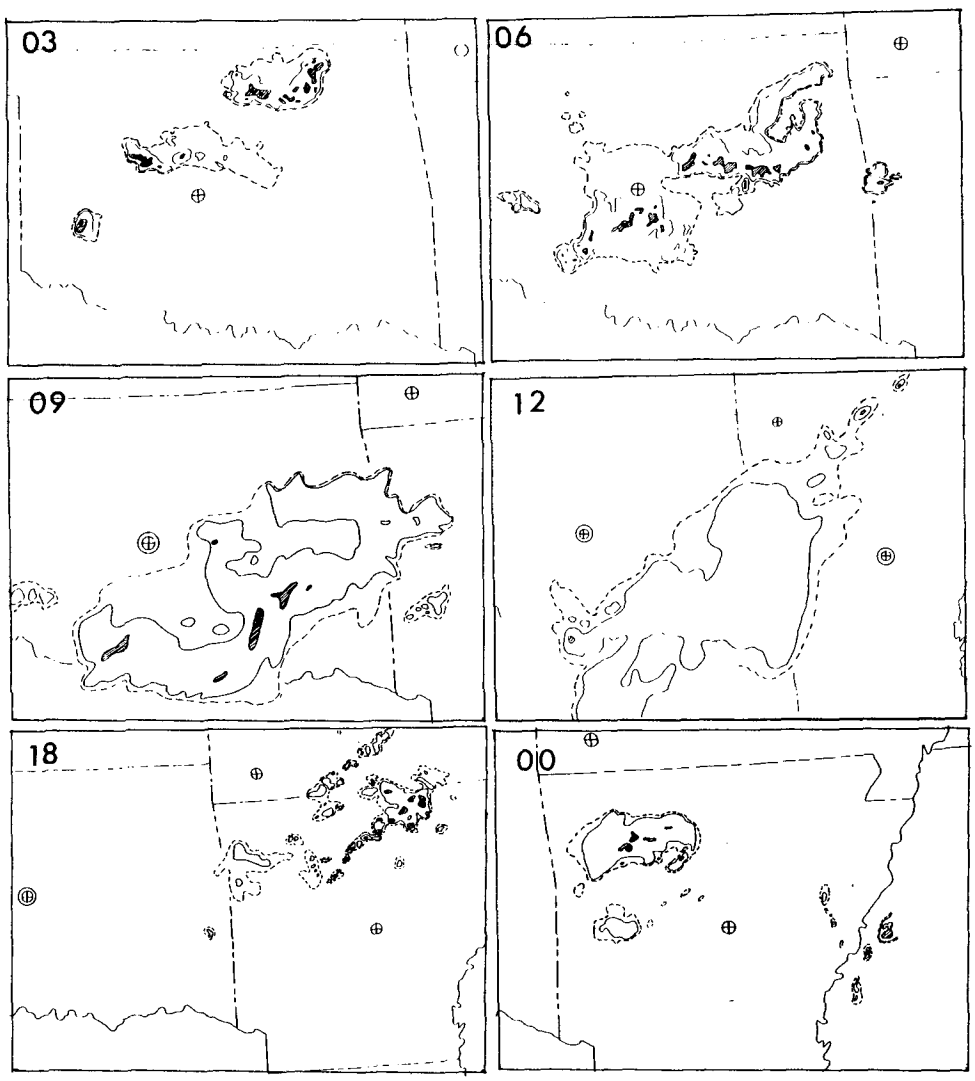

FIG. 7b. The composite analysis of radar echoes for the period 0300 UTC 7 July–0000 UTC 8 July 1982. The dashed and solid lines, light and dark shadings denote level-1, -2, -3 and -4 radar echoes, respectively. The circles are the location of radar observation sites.

mation field, provided a favorable along-front forcing for lifting air parcels to the level of condensation. However, due to the coarse resolution and smooth initial conditions, the low- to midlevel circulation and thermodynamic conditions associated with the model front are not as sharply defined as in nature. It took more than 3 model h for the front to assume a strength and distribution comparable to the observations. This is also the approximate period for the parameterized convection to become well distributed along the front. In this sense, and considering the fact that the observed squall line formed 1–2 h prior to the model integration time, there is a little delay in the generation of diabatic heating and the organization of the model MCS during the first 12 h. To facilitate later discussion on the evolution of the surface features and the vortex, Fig. 7a shows the simulated hourly implicit and explicit precipitation rate as a function of time, and Fig. 7b shows a composite analysis of radar echoes for the period 0300 UTC 7 July–0000 UTC 8 July. The implicit rainfall rate increases very rapidly during the initial model adjustment period, and reaches its maximum around 0400 UTC. The explicit convective scheme did not begin to produce precipitation until 0300 UTC (i.e., 3 h into the simulation).

During the period 0000–0600 UTC, the MCS was gradually losing its line structure and becoming more compact (see Fig. 6). According to Maddox (1980; 1983), this is evidence of rapid intensification of the MCS. At the surface, mesoscale high-pressure perturbations and cold outflow boundaries associated with the MCS gradually developed, and obscured the frontal pressure trough zone (see Fig. 8). In the model, the parameterized moist downdrafts [see a typical heating profile in Zhang and Fritsch (1986a)], evaporative cooling and melting are able to generate such mesohighs (see Zhang and Fritsch 1986a; Zhang et al. 1988; Zhang 1989). However, because of the delay in the development of the model squall line, the convectively produced pressure perturbations lagged the observed. The model mesohigh did not become evident until 1200 UTC when there was enough cold air generated beneath the model MCS. On the other hand, it may be that the scale of the observed pressure perturbations associated with the MCS was a little too small to be resolved with the present grid resolution. Note, however, that the simulated position of the frontal system, the distribution of the deep convection, and the cold outflow boundary are similar to the observed.

By 0900 UTC, the MCS has undergone considerable intensification and expansion and its satellite-observed cold cloud shield has met the MCC size criteria defined by Maddox (1980). Note that the MCS, which was linearly oriented along the surface front a few hours ago, now has become circularly configured (Fig. 6). Very interestingly, the simulated MCS also evolves from a line structure to a more circular structure, and its location and size are comparable to the observations

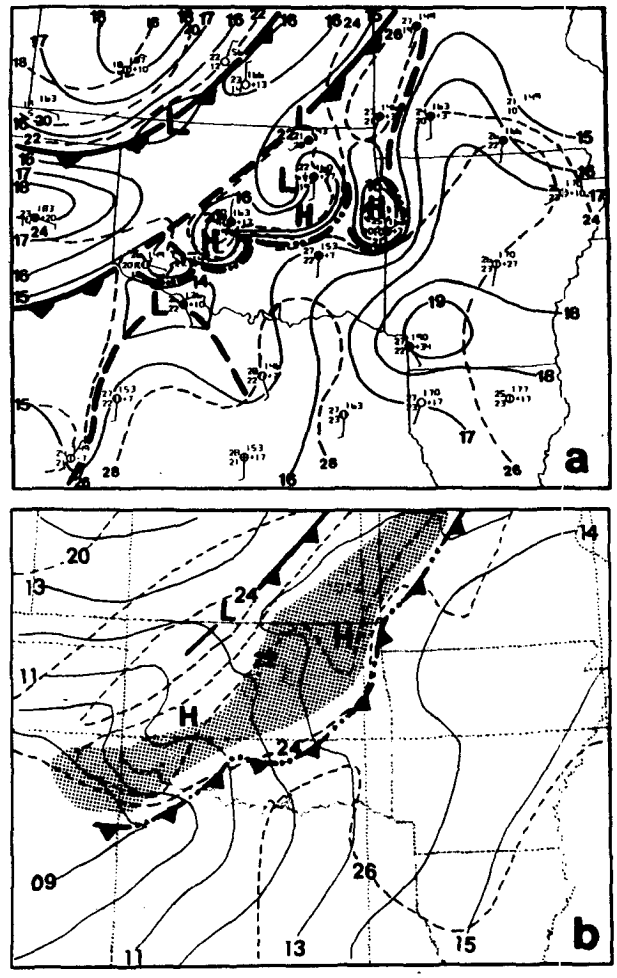

FIG. 8. Mesoscale analysis for 0600 UTC 7 July 1982. Solid lines are isobars (mb). Long-dashed lines with double dots denote the locations of outflow boundaries. (a) Observational analysis adapted from Menard (1988). A full wind barb is 5 m s^{-1}. (b) Model simulation. The dashed lines are surface temperature (°C). Shading denotes the area of active convection produced by the implicit convective scheme.

(see Fig. 9). However, the implicit rainfall rate only increases slightly. This qualitatively conforms to the radar echo analysis in which the area of level-3 and -4 returns actually decreased with time (Fig. 7b). The longitudional compaction and lateral expansion apparently are related to the interaction of the downdraft outflow with high energy influx by the low-level jet (i.e., the combination of the low-level jet with the high-θ_e air; see Figs. 3 and 8). During this period, the low-level jet appears to be lifted over the cold outflow. And in a sensitivity experiment in which the parameterized moist downdrafts were omitted, little lateral expansion and longitudional compaction occurred (not shown). The lateral expansion of parameterized convection appears to have assisted the rapid generation of explicit condensation hereafter (see Fig. 7a). In particular, the

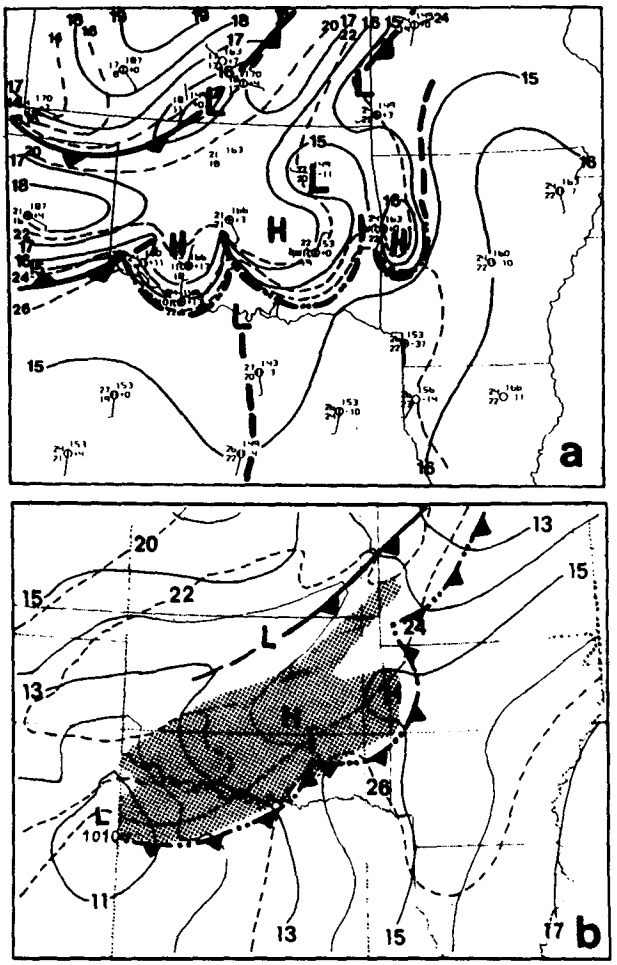

FIG. 9. As in Fig. 8 but for 0900 UTC 7 July 1982.

increase in the area of convective overturning helps enhance mesoscale convergence, and thus facilitates the adjustment of the atmospheric stratification in the central part of the MCS toward a moist adiabatic and saturated condition [see discussions in Zhang and Fritsch (1987, 1988)]. The centralized mesoscale ascent in combination with nearly moist adiabatic and satuarated conditions has been found to be favorable for the genesis of mesovortices (Zhang and Fritsch 1986b).

Satellite imagery indicates that the MCS reached its greatest size and intensity around 1000 UTC (see Menard et al. 1986) and then gradually weakened. Presumably, this is also about the time that the embedded mesovortex was developing near the center of the MCC. However, in the model, the explicit precipitation, which is considered to be responsible for the spinup of the vortex circulation (Leary and Rappaport 1987; Zhang and Fritsch 1987, 1988), just begins to rapidly accelerate at this time and attains the maximum rate at 1200 UTC (Fig. 7a). In this regard, such a delay in the latent heat release may affect the timing of the generation of a midtroposperic warm-core mesovortex in the model.

The evolution of the cold cloud shield and the sea level pressure pattern from 0900 to 1800 UTC (see Figs. 6 and 9-11) indicates that the MCS tends to split into two parts: one propagates southward into the warm moist air flowing northward across Texas, and the other moves northeastward parallel to the surface frontal zone. As mentioned before, the lifting of warm moist air by the cold downdraft outflow was a key factor in initiating new convection, particularly on the southern flank of the system. The model reproduced reasonably well the sea level pressure pattern, location of the frontal system and the pattern of the main convective system (see Fig. 10). The simulated MCS also tends to split over southeastern Oklahoma at this time. However, the model falsely produces an area of convection over the cold outflow near the southwestern boundary of the subdomain. The overgeneration of convection in this region appears to be largely due to some uncertainties in the initial conditions. Specifically, the model

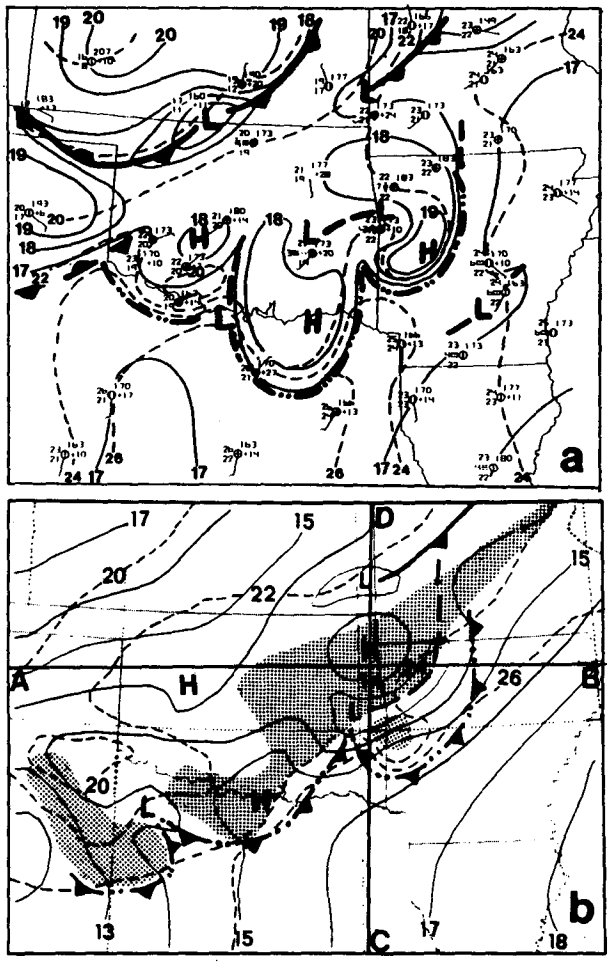

FIG. 10. As in Fig. 8 but for 1200 UTC 7 July 1982.

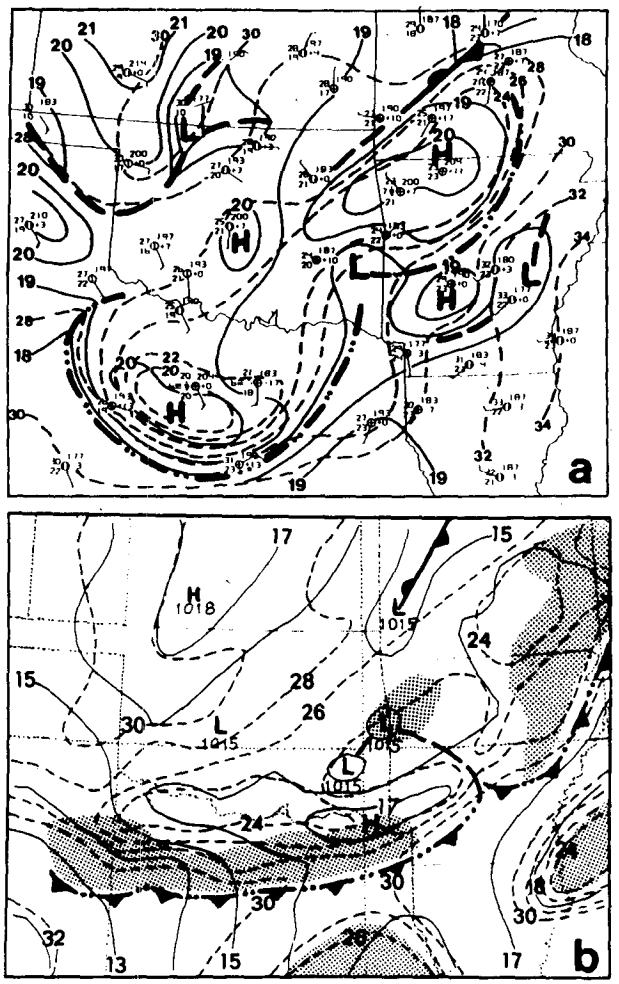

FIG. 11. As in Fig. 8 but for 1800 UTC 7 July 1982.

atmospheric information entering the fine-mesh domain through the lower-level southerly or southwesterly flow is from either a no-data-enhancement region (e.g., over the ocean) or a data-void area (e.g., over southwestern Texas and northern Mexico), as can be seen from Fig. 3. Such uncertain information seems to have propagated into the surroundings of the MCS around this time, and seriously affected the forecast accuracy of some important features (e.g., the southward propagating convective system and the low- to midlevel mass and wind fields) at later model hours. The simulated northeastern convective development is considered to be reasonable as compared to satellite imagery since convection at most of the grid points is found to be weak and shallow, and formed in response to the early morning surface heating. Note that a distinct meso-β scale high pressure has formed at the Oklahoma–Missouri–Arkansas border. But it is located a little too far to the north, as compared to observations. The development of the mesohigh in the model is a result of the combined effects of the parameterized cold downdrafts, the resolvable-scale evaporative cooling and hydrostatic water loading in the low to midlevels (see Zhang et al. 1988; Zhang and Fritsch 1988). The last two effects are consistent with the fact that the explicit precipitation rate reaches its maximum at 1200 UTC (see Fig. 7a). A more detailed discussion of the role of the explicit precipitation will be presented in part II of this paper. The mesolow centers to the north and south of the mesohigh are more transient than the mesohigh and may form from mesoscale compensating subsidence or possibly as a result of gravity wave forcing as the flow impinges upon the cool pool. This will be shown in subsection 4b. The failure of the model to reproduce the observed low along the Kansas–Oklahoma border can not be readily explained. It may be due to the coarse-resolution initial conditions.

After 1200 UTC 7 July, both observations and the simulation indicate weakening and a quasi-stationary nature of the mesovortex. In particular, satellite imagery (visible and infrared) shows a decrease in cloudiness and in the circular contiguous cloud shield (see Fig. 6). The radar echoes also exhibit the trend of disorganization with a decreasing level of returns and areas (Fig. 7b) while the simulated explicit rainfall rate diminishes with time (see Fig. 7a). As shown by Menard et al. (1986) and later in this section, this is because 1) the rotating MCS was moving into a much more thermodynamically stable regime, and 2) drier and colder air entered the vortex circulation system through cross-frontal flow. The lowering of equivalent potential temperature by the parameterized moist downdrafts and the interception of the lower-level energy supply by the southward propagating component of the MCS may also have contributed to the weakening of the entire system.

Examination of the model results reveals that the strongest low-level jet always accompanies the vortex due to its low central pressure and the resulting tight pressure gradient. This will be shown in subsection 4b. Apparently, the jet tends to create an area of divergence to the south of the vortex which is unfavorable for the maintenance of convection and continued convective development, and an area of convergence northeast of the vortex which helps the MCS move into northern Arkansas. The unfavorable flow condition appears to be partly responsible for the decay of the southward propagating cloud system hereafter, as indicated from both observations and the model simulation.

It is of particular interest that the dissipation of the upper-level cold cloud shield allows visual observation of the low- to midtropospheric circulation. During 1500 to 1800 UTC, a low- to midlevel cyclonically rotating cloud system (mesovortex) is clearly visible at the Oklahoma and Arkansas border (see Fig. 6). The center of the vortex circulation is situated nearly over the observed and model-simulated surface mesolow centers (cf. Figs. 6 and 11). Subsequent to this time period, both observed and simulated sea level pressure pertur-

bations associated with the mesovortex gradually flatten. For example, at 0000 UTC 8 July (i.e., 24 h into the simulation), the simulated low pressure perturbation is nearly negligible beneath the vortex (see Fig. 12). The Menard surface mesoanalysis for 1200 UTC 8 July also displays virtually no surface low pressure perturbation associated with the rotating MCS (not shown). This is significantly different from other case studies of mesovortices in which a distinct and persistent surface mesolow often appeared at a later stage of the vortex development (Rockwood et al. 1984; Zhang and Fritsch 1986a, 1987).

At 0000 UTC 8 July, the model still reproduces some aspects of the mesoscale sea level pressure pattern and the boundary layer thermodynamic conditions. In particular, the model maintains the trough/outflow boundary stretching from central Texas northeastward into Arkansas, and the front through southeastern Kansas. It is also noteworthy that the area of (weak) major convection over northwestern Arkansas is about at the right place, indicating that the area of simulated

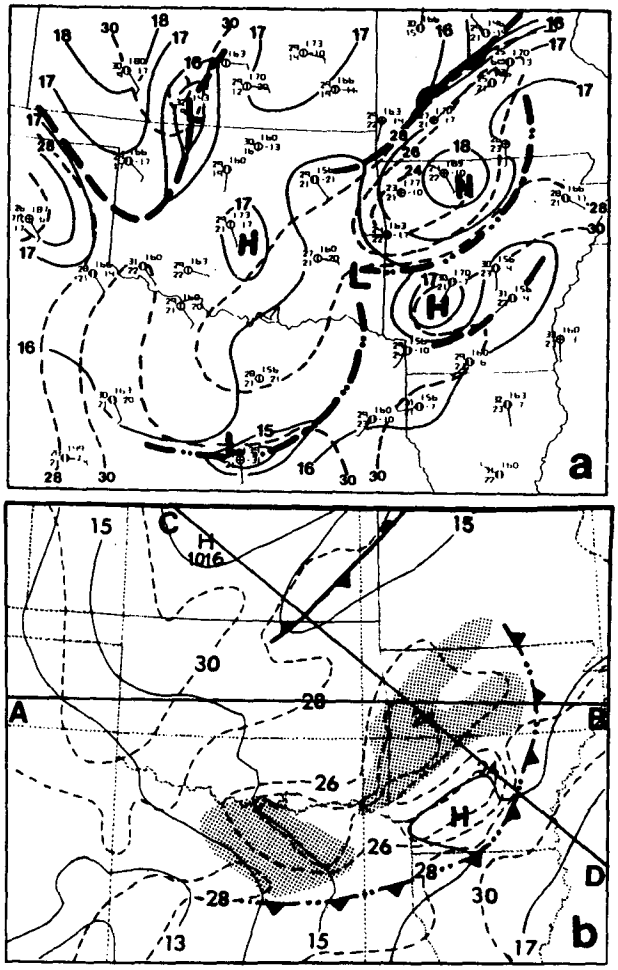

FIG. 12. As in Fig. 8 but for 0000 UTC 8 July 1982.

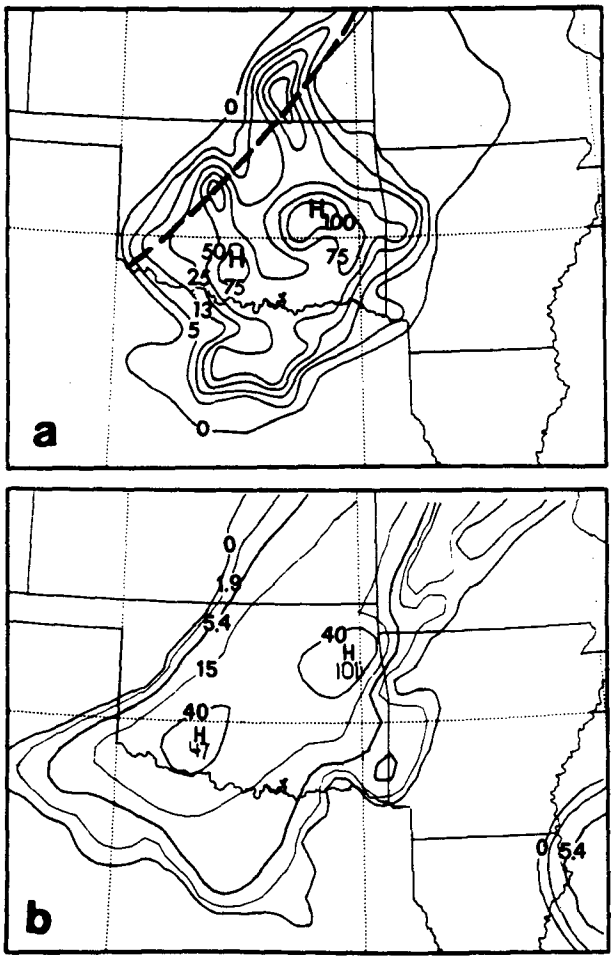

FIG. 13. Comparision of (a) the observed rainfall (mm) for 1200 UTC 6 July–1200 UTC 7 July (adapted from Menard et al. 1986) with (b) the predicted for 0000–1200 UTC 7 July 1982. The dashed lines in (a) are drawn to approximately partition the accumulated rainfall before (left side) and after (right side) 0000 UTC 7 July.

mesoscale ascent and convectively favorable environmental conditions over this region are comparable with the observations.

Before examining the corresponding tropospheric structure and evolution of the vortex in subsection 4b, it is important to see if the model reproduced the magnitude and distribution of the rainfall associated with the rotating MCS. Figure 13 compares the simulated first 12-h (0000–1200 UTC 7 July) accumulated rainfall with the observed 24-h (1200 UTC 6 July–1200 UTC 7 July) analysis. The 24-h observed amounts are shown because this analysis is based upon the high density River Forecast network of observations and provides the most possible detail about the actual precipitation. It is important to point out that the model initial time (0000 UTC 7 July) lagged by more than 2 h the observed initiation of the squall line. It is also important to note that the observed 24-h amounts only

include precipitation from the MCS under investigation. The heavy dashed line in Fig. 13a shows the approximated position of the squall line at 0000 UTC 7 July (see Fig. 6). Therefore, almost all of the precipitation southeast of this line was generated between 0000–1200 UTC 7 July. It can be seen that the model-produced rainfall pattern and magnitude conform reasonably well to the observations. The model-accumulated resolvable-scale precipitation accounts for 11%, 37% and 24% of the rainfall totals during the period 0000–1200 UTC 7 July, 1200 UTC 7 July–0000 UTC 8 July, and 0000 UTC 7 July–0000 UTC 8 July, respectively (not shown, but can be seen from Fig. 7a). The actual percentage of the resolvable-scale rainfall associated with the vortex is higher since the simulated convective rain unrelated to the MCS has been included in the calculation. In fact, Fig. 7a shows that the resolvable-scale rainfall rate during the mature stage (i.e., from 1000–1600 UTC 7 July) is significantly larger than the parameterized precipitation rate. The acceleration of the resolvable-scale rainfall during 0800–1200 UTC 7 July corresponds to the intensification of the vortex in the model. Because of the delay in the grid-box saturation by the mesoscale ascent, the model probably underestimated the resolvable-scale rainfall during the first 12 h and overestimated it during the second 12 h period. The significant percentage of the resolvable-scale (or stratiform) rainfall is consistent with many observational and numerical studies of MCCs and tropical cloud clusters (e.g., Houze 1977; Churchill and Houze 1984; Perkey and Maddox 1985; Smull and Houze 1987; Zhang and Fritsch 1987; Leary and Rappaport 1987).

b. Evolution of the mesovortex circulation structure

Figure 14a shows the simulated time evolution of the maximum relative vorticity profile obtained from each level at the circulation center. For the convenience

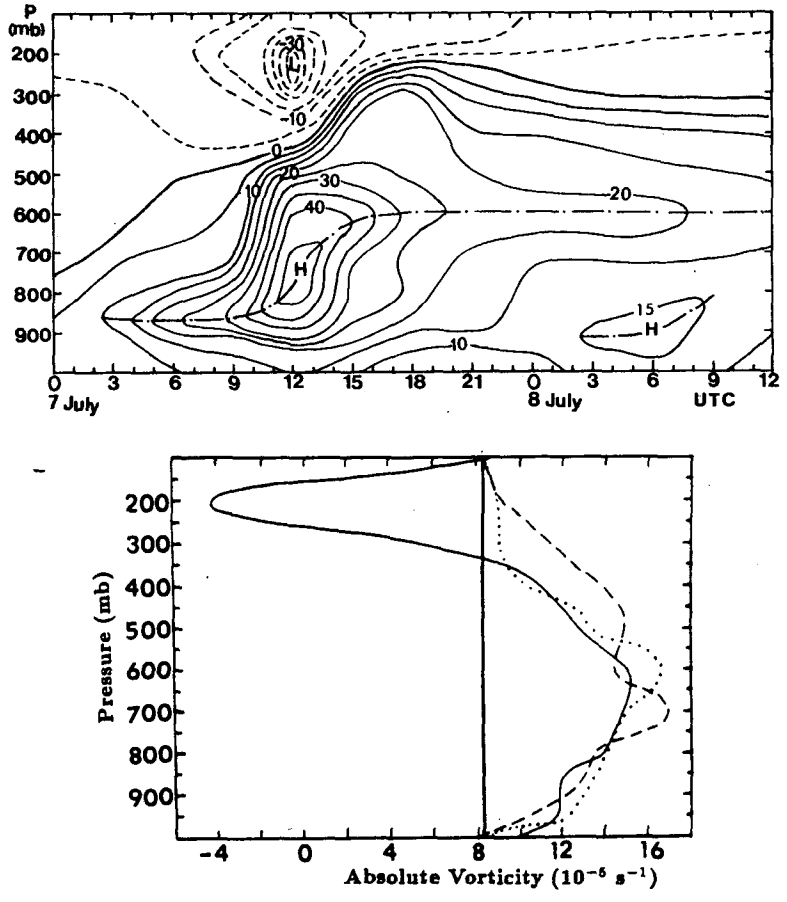

FIG. 14. (a) The time evolution (0000 UTC 7 July–1200 UTC 8 July) of the vertical distribution of the simulated maximum relative vorticity (10^{-5} s^{-1}) at the vortex circulation center; (b) Diagnostic absolute vorticity profiles (10^{-5} s^{-1}) for 1200 (solid), 0000 (dashed) and 1200 (dotted) UTC 7–8 July (adapted from Menard et al. 1986). The thick solid line denotes vanishing relative vorticity.

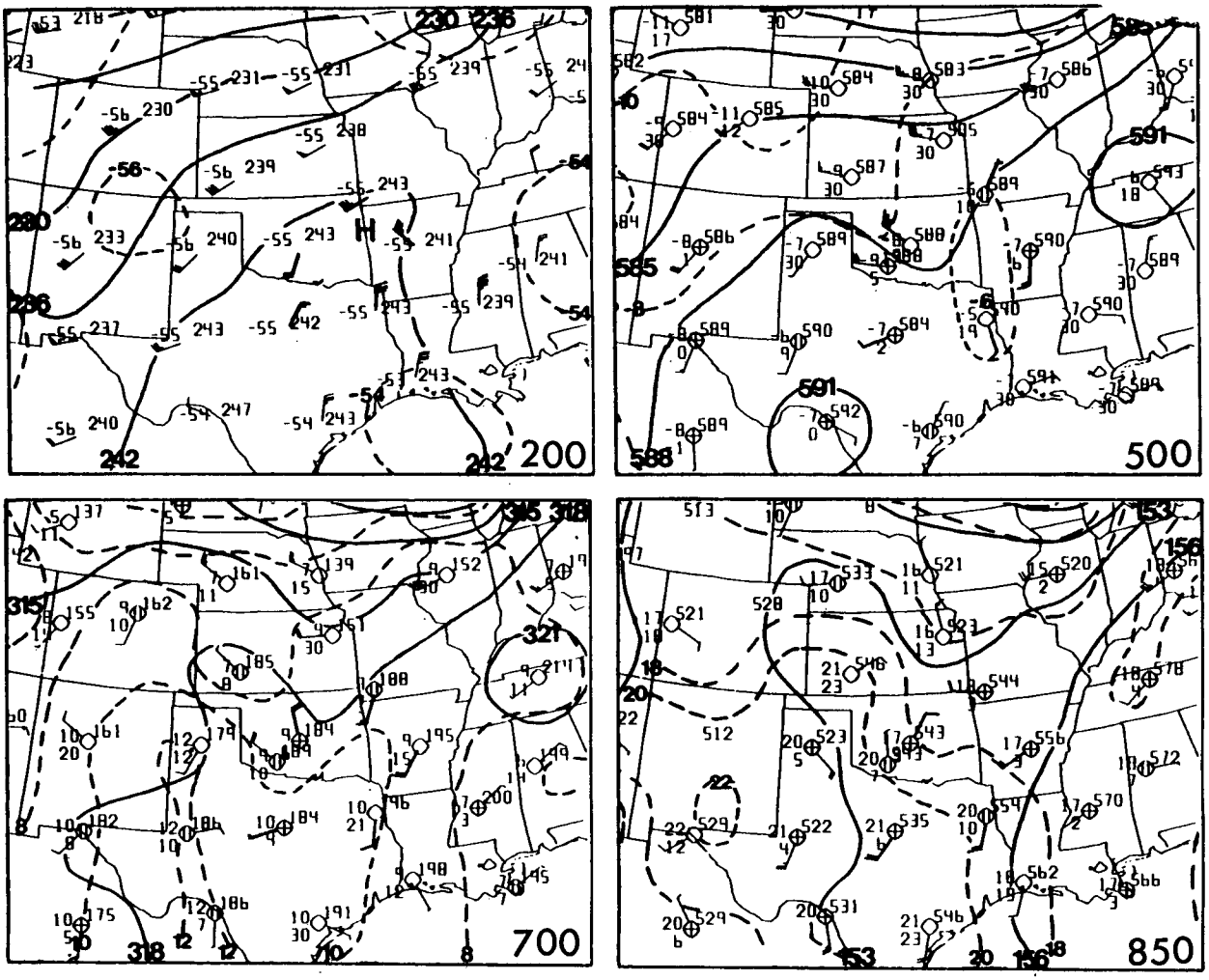

FIG. 15a. Upper air analyses of height (solid lines), temperature (dashed lines), dewpoint and horizontal winds for 1200 UTC 7 July 1982 (adapted from Menard 1988). Wind speed is in m s^{-1} with a full barb of 5 m s^{-1}.

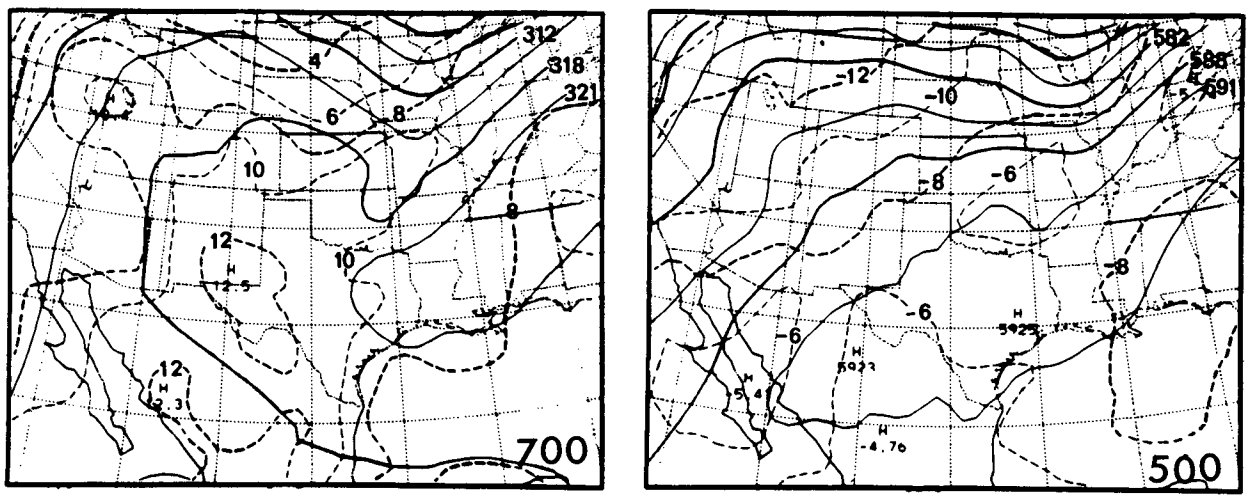

FIG. 15b. Twelve hour forecast of height (solid lines) and temperature (dashed lines), valid at 1200 UTC 7 July 1982.

of later discussion, Fig. 14b shows the diagnostic vorticity profiles obtained by Menard et al. (1986) for 1200 UTC 7 July and 0000 and 1200 UTC 8 July. Initially, as shown in Fig. 3, there is a horizontal shearing zone accompanying the low-level frontal system, and mid- to upper levels are basically dominated by westerly and southwesterly flow. Thus, the maximum cyclonic vorticity was initially concentrated at low levels with one center situated over north-central Texas (Fig. 2a) and another associated with the short wave to the north of the area where the rotating MCS was developing. Twelve hours later, in response to the rapid acceleration in the resolvable-scale latent heat release, the maximum relative vorticity quickly ascended to the 750 mb level where its value reached 45×10^{-5} s^{-1}. Meanwhile, significant anticyclonic vorticity appears near the tropopause. It is of particular significance that the maximum vorticity stays around 600 mb hereafter and very slowly decays, whereas the upper-level anticyclonic vorticity quickly returns to values characteristic of the pre-MCS environment. The simulated time evolution of this vorticity profile agrees quite well with the diagnostic computations by Menard et al. (1986), but the simulated values are larger (cf. Figs. 14a, b). This is probably due to the use of the high resolution of the model grid relative to the coarse-resolution rawinsonde data used by Menard et al. (1986), particularly for the 1200 UTC 7 July profile in which the vortex was located near the center of four rawinsonde stations (see Fig. 2b). Note in Fig. 14a that a secondary vorticity maximum emerges after 0000 UTC 8 July. This appears to correspond to the redevelopment of lower-level stratiform clouds (see Fig. 6).

The model verification that follows below will mostly concentrate on the *immediate meso-β and larger scale environment* (i.e., the subdomain of the fine mesh) associated with or being essential to the rotating MCS. Figures 15–18 compare the model-simulated upper-air features valid at 1200 UTC 7 July to the Menard analysis and other related data. Figure 19 shows various model cross sections of vertical motion (ω), potential temperature (θ), equivalent potential temperature (θ_e), and relative vorticity and circulation vectors along the cross-sectional plane. For the display of the short-wave structure, the 700 mb (or 500 mb when necessary) level will be shown since, like the 1977 Johnstown mesovortex case (see Zhang and Fritsch 1986a, 1988), the 700 mb level has been found to be the approximate level where the maximum wave amplification occurs in both observations and the model simulation.

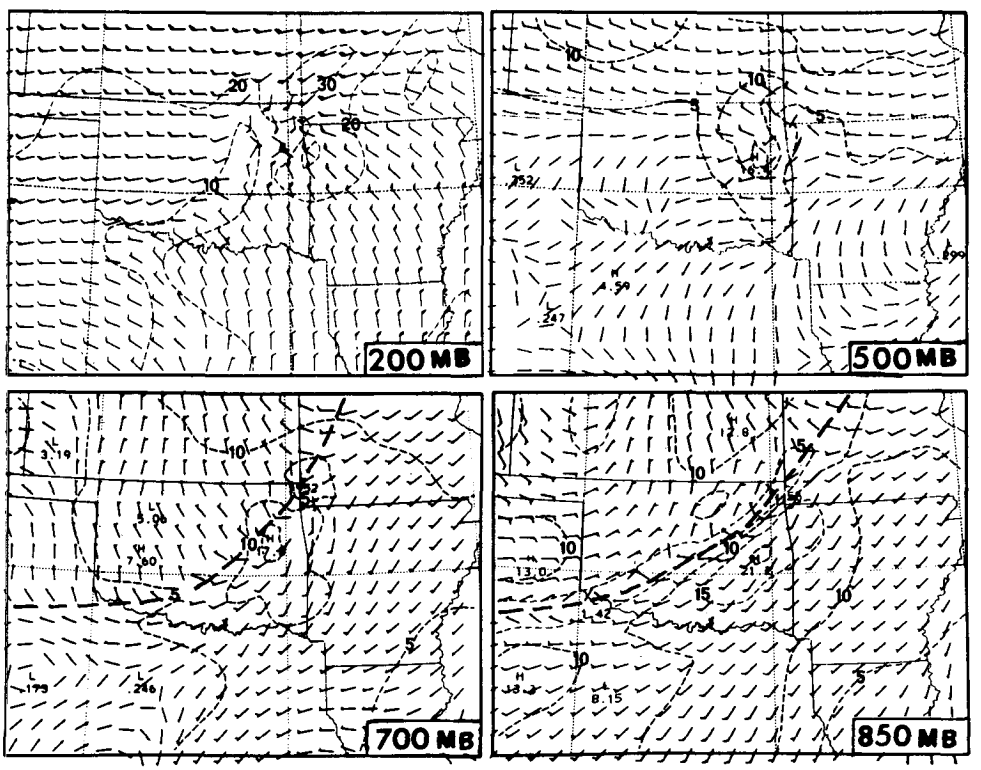

FIG. 16. Twelve hour forecast of mesoscale wind field at every other grid point for 1200 UTC 7 July 1982. Dashed line denotes isotach (a full barb is 10 m s^{-1}). Heavy dashed line indicates axis of short-wave trough or low-level frontal zone.

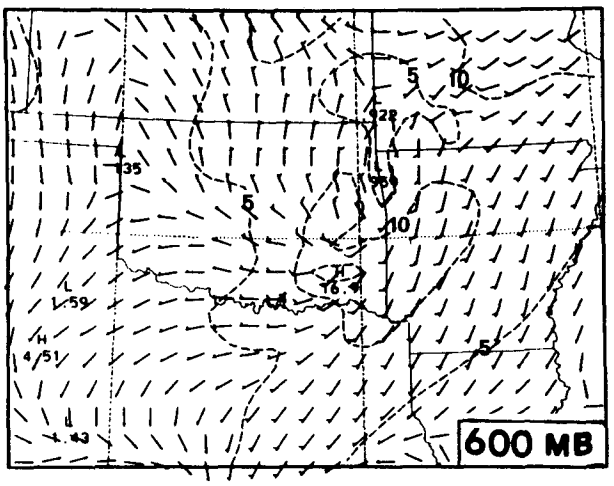

FIG. 17. As in Fig. 16 but for 15 h forecast of 600 mb wind field, valid at 1500 UTC 7 July 1982.

Comparison of Figs. 3 and 15a indicates that the short-wave trough (at 500 and 700 mb) accompanying the MCS greatly amplified from 0000 to 1200 UTC 7 July. In addition to hydrostatic height falls within the vortex in the low to midlevels, a significant wind perturbation with a local warm-core temperature anomaly at 500 mb has also developed. The 500 mb wind at station UMN, Missouri reveals a substantial departure from geostrophic balance. Moreover, near the tropopause, an anticyclonic wind circulation corresponding to the cold cirrus cloud shield in Fig. 6 becomes clearly apparent over the region of the rotating MCS (cf. Figs. 3 and 15a). Similar anticyclonic wind patterns have also been observed and simulated as an important characteristics of MCCs in other case studies (e.g., Fritsch and Maddox 1981; Maddox et al. 1981; Wetzel et al. 1983; Zhang and Fritsch 1987).

In general, the simulated immediate environment of the rotating MCS at 1200 UTC 7 July conforms to the observational analyses (cf. Figs. 15a, b). In particular, the model reproduces well the location and amplitude of the 700 mb short-wave trough and 500 mb warm-core structure associated with the rotating MCS. The predicted surrounding temperature and height distributions also agree reasonably well with the observed ones. The warm core, as mentioned by Zhang and Fritsch (1987), results from the surplus of latent heat release over the adiabatic cooling and horizontal energy dispersion. The amplification of the short-wave trough in association with the mesovortex is consistent with many observational studies in which a weak midtropospheric short wave often accompanies the genesis of MCCs (Hoxit et al. 1978; Maddox 1983; Bosart and Sanders 1981; McAnelly and Cotton 1986). In the case of the 1977 Johnstown MCSs, a meso-α scale short wave assisted the generation of the mesovortex, and the mesovortex, in turn, helped to enhance the short wave [a positive feedback process (see Zhang and Fritsch 1986a,b, 1988)]. However, in the present case, it appears that the short wave did not play a very significant role since the initial short-wave forcing was extremely weak and located too far to the north. Furthermore, the model was unable to produce the height perturbation over northeastern Oklahoma in sensitivity experiments in which the mesovortex did not take place. Above 700 mb, both the predicted and observed short waves tend to lose their perturbation structure owing to the presence of a warm-core temperature anomaly aloft, as has also been demonstrated by Zhang and Fritsch (1986a).

Figure 16 shows the simulated mesoscale flow fields at 850, 700, 500 and 200 mb levels at 1200 UTC 7 July and should be compared to those in Fig. 15a. The observed horizontal wind deformation and cross frontal flow at 850 mb, the significant wind perturbation in the midtroposphere (i.e., 700 and 500 mb) and mesoanticyclone near the tropopause are all well reproduced. Both observations and the simulation show that the strongest cyclonic wind perturbation occurred around 700 mb. This apparently is a result of the occurrence of maximum amplification of the short-wave trough at this level. The model also produced some nonobserved—but very plausible—features associated with the rotating MCS. These include 1) the enhanced low-level southwesterly flow ahead of the front with strong mass convergence over northwestern Arkansas; 2) generally stronger westerly wind south of the vortex within most of troposphere; 3) an upper-tropospheric "obstacle" effect which slows down air parcels approaching the vortex and then forces them to divert around it; and 4) the development of the high-level jet streak to the northeast of the vortex. Based upon the satellite imagery, the observed MCS appeared to be in its most intense stage (see Maddox 1980) around 1000 UTC. Shortly thereafter (1200 UTC), both observations and the simulation exhibited a very weak closed cyclonic wind circulation only around 500 mb (Figs. 15 and 16). As mentioned by Zhang and Fritsch (1987), the closed wind circulation is a consequence of a rapid geostrophic adjustment of the wind field towards the perturbed mass field. A closed geostrophic wind circulation began to develop in most of the model troposphere between 1000 and 1100 UTC. It took more than 3 h for the actual winds to adjust to the warm-core temperature perturbation. Thus, Fig. 17 shows the predicted 15-h horizontal wind field at 600 mb. The 600 mb level is used here because this is the level where the closed meso-β scale cyclonic wind circulation is best defined in the model; this is also the level where both observed and simulated local maximum cyclonic vorticity is approximately located hereafter (see Menard et al. 1986 and Fig. 14 herein). Note that the circulation elongates along the trough axis. The elongated

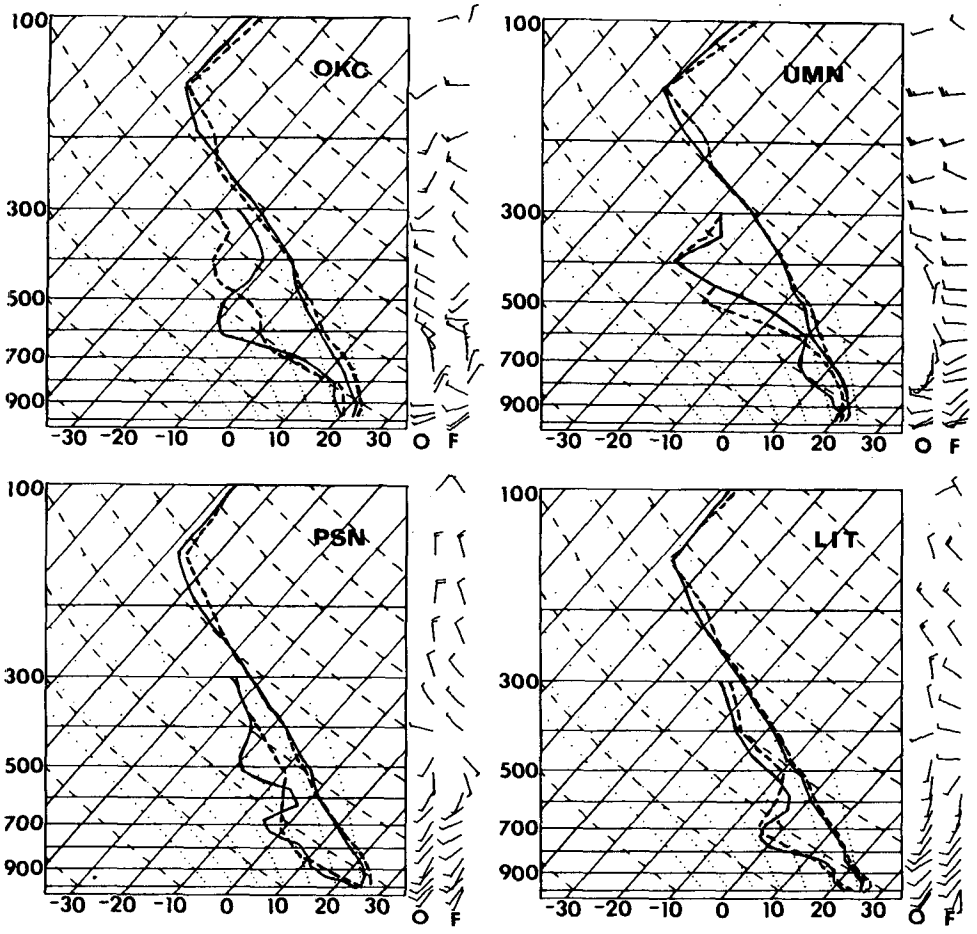

FIG. 18. Upper-air sounding comparisons of the observed (solid lines) with the simulated (dashed lines) for 1200 UTC 7 July 1982 (see Fig. 2 for the locations). The letters *O* and *F* denote the observed and simulated winds, respectively. A full barb is 10 m s^{-1}.

characteristic corresponds to the distribution of diabatically forced vertical motion along the frontal zone and is more likely a result of the horizontal advection by the deformation winds along the dilation axis. This feature also appears in most of the other meteorological variables (e.g., equivalent potential temperature, vorticity, precipitable water, etc.). From 700 mb downward, both the observed and simulated wind perturbations are basically dominated by cyclonic cross-frontal flow along the frontal zone.

To further show the model's capability of predicting the vortex environment, Fig. 18 compares observations and forecasts of four upper-air soundings encircling the mesovortex at 1200 UTC. The model reproduces very well the vertical profiles of temperature, dew point and winds ahead of the low-level frontal system (e.g., stations PSN, Texas and LIT, Arkansas). The successful duplication of the vertical thermal and wind structure, particularly within the lower-level southwesterly flow can be considered as substantial evidence that the model has generated the long-lived MCS at nearly the right place and time. On the other hand, the model produced excessive warming below 500 mb at OKC in Oklahoma, and too much moistening below 600 mb at UMN in Missouri. Moreover, the predicted midtropospheric wind profiles at these two stations differ somewhat from the observed. Note, though, that these disagreements might be attributed to the fact that the frontal zone (with sharp gradients) is about to pass by (UMN, Missouri) or has passed by (OKC, Oklahoma) so that a few tens of kilometers difference between the simulated and observed frontal position could make significant departures in dynamic and thermodynamic properties. Of course, any deficiency in the initial conditions, model physics and numerics could also contribute to such disagreements.

Since the model simulation reproduced reasonably well many of the observed mesoscale features, the simulated vertical structure can now be examined with more confidence that it is physically meaningful. In

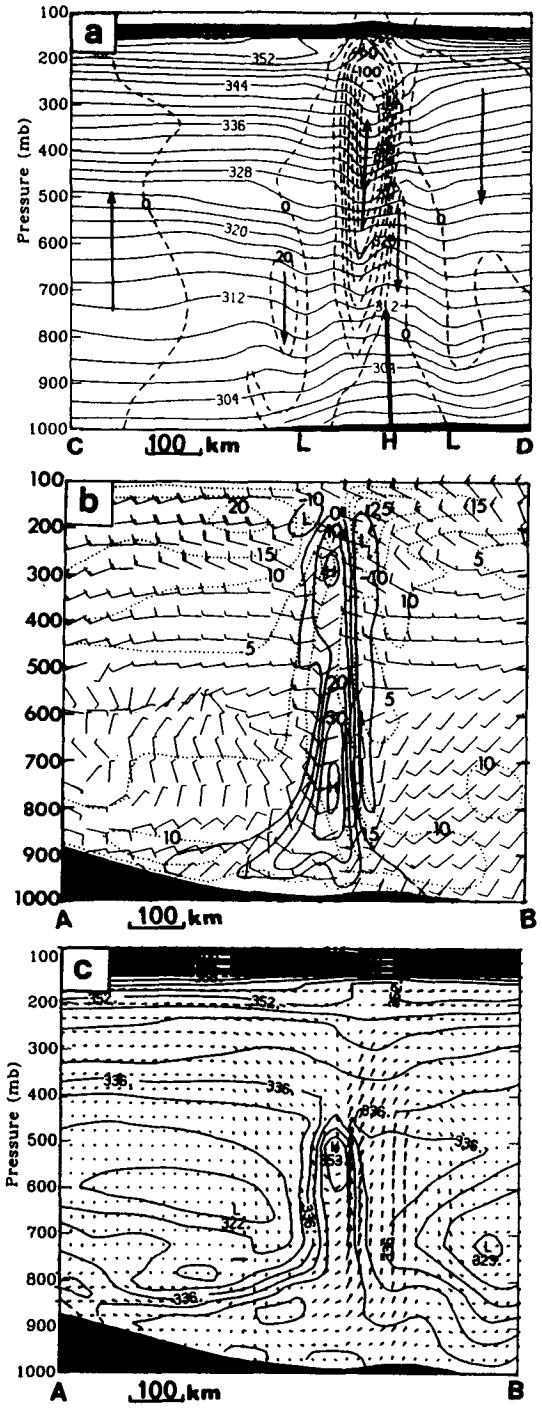

FIG. 19. (a) Vertical cross section of potential temperature (solid lines at intervals of 2 K) and ω (dashed lines at intervals of 20 μb s^{-1}) along line CD in Fig. 10 (12 h forecast). Arrows denote direction of vertical motion and H and L denote surface mesohigh or mesolow, respectively. The heavy solid line above the mesohigh indicates the vertical axis of the vorticity maximum along this section. (b) Vertical cross section of horizontal wind (speed, m s^{-1}; direction, common convention) and relative vorticity (solid lines at intervals of 10×10^{-5} s^{-1}) along line AB in Fig. 10 (12-h forecast). Dotted lines are isotachs with intervals of 5 m s^{-1}. A full barb is 10 m s^{-1}. (c) Vertical cross section of equivalent potential temperature (solid lines at intervals of 4 K) and circulation vectors along the cross-sectional plan which is taken along line AB in Fig. 10 (12-h forecast).

particular, comparision of Figs. 3, 5 and 19 shows tremendous intensification of vertical motion and concentration of cyclonic vorticity associated with the developing vortex. Note that except for the 150 mb layer at the top and bottom of the model, the horizontal scale of the disturbance is about 150 km. The maximum upward motion, which takes place between 400 and 300 mb, exceeds 140 μb s^{-1}. Menard (1988) also diagnosed this maximum upward motion near 300 mb from observations. As discussed in Zhang and Fritsch (1987, 1988), such a strong upward motion is most likely produced by the resolvable-scale condensation since, near the vortex center, the atmospheric stratification is close to a satuarated and moist adiabatic condition; i.e., the contribution of sensible eddy fluxes to the parameterized convective heating is relatively small. It is important to point out that the maximum upward motion, as well as the maximum temperature perturbation, is located at a higher level than that previously reported. This shift to a higher level appears to result from the incorporation in the model of evaporative cooling, hydrostatic water loading, ice melting, and parameterized moist downdrafts. Specifically, these processes tend to reduce grid-scale condensation heating and retard the development of unrealistic mesoscale upward motion, particularly at lower levels (see Zhang et al. 1988), because at upper levels only slight evaporation and water loading can be operative. In fact, the vortex circulation below 800 mb is basically dominated by sinking motion, which corresponds to a pool of cool air produced by the above-mentioned processes. It is evident that this cool pool is responsible for the generation of the mesohigh over northeastern Oklahoma (cf. Figs. 10b and 19a). It is also apparent now that the transient mesolows to the north and south of the mesohigh (see Fig. 10) are due to the presence of mesoscale subsidence. Above the cool pool, an apparent warm-core structure, being in phase with the centralized upward motion, extends up to 250 mb where a changeover to a cold dome occurs. The coldest observed temperature in the fine-mesh domain (≤ -70°C) was found at UMN in Missouri. This cold dome is generated in the model primarily through a continued transport of large amounts of mass by the mesoscale ascending circulation. This mass then spreads out in a thin layer near the tropopause, and subsequently influences the environmental flow of the vortex over an extensive area. The simulated high-level mesohigh and the corresponding anticyclonic circulation (see Fig. 16) are found to form at a much earlier time and larger scale in the model than the low- to

midtropospheric cyclonic circulation. This is likely due to the greater tendency of the adjustment of winds toward the perturbed mass field when the scale of motion is closer to the Rossby radius of deformation. McAnelly and Cotton (1986) also observed the development of an anticyclonic circulation within a thin layer during the mature stage of an MCC. It is of particular interest that the horizontal spreading of this cold air mass also leads to a lifting of the tropopause at a scale much larger than the vortex (cf. Figs. 19a and 6). This feature is consistent with the often observed cold cloud shields ($T \leq -62°C$) in satellite imagery associated with MCCs and with the anticyclonic perturbations observed in the regular network of sounding data (e.g., see Fritsch and Maddox 1981).

Note in Fig. 19 the relative configuration of the strongest vertical motion and vorticity with respect to the surface pressure perturbation. The strong upward motion and low-level convergence occur ahead of the maximum vorticity column. This is also apparent by visually examining the 850 mb wind field (see Fig. 16) in which the cross-frontal wind perturbation attains the maximum cyclonic vorticity along the frontal zone but strong convergence appears ahead of the front. *Thus, the phase difference between the vorticity and convergence may be an important component of the propagation mechanism of the developing mesovortex and associated frontal system.* Note also that the high-θ_e core also lags behind the maximum upward motion (and high-θ core region). The phase difference between θ and θ_e implies that the propagating mesoscale ascent brings in low-level moisture which is subsequently trapped within the trailing region of strong cyclonic vorticity. This can be explained, using an inertial stability argument, that the large inertial stability provides resistence to the radial displacement of moisture-carrying parcels, whereas it favors the tangential and vertical displacements (see Smith 1981; Schubert and Hack 1982; Hack and Schubert 1986). However, the upward motion and vorticity are found to be nearly in phase when both implicit and explicit convections are omitted (not shown); this is similar to the results in the numerical simulation of an observed cold front by Orlanski and Ross (1984) and Ross and Orlanski (1982).

Like the 1977 Johnstown mesovortex case, the model produced a column of uniformly distributed horizontal momentum and equivalent potential temperature coincident with the vortex. Observed winds at UMN also indicate the relative uniform distribution of horizontal momentum up to 300 mb (see Fig. 18). As pointed out by Zhang and Fritsch (1987), the vertical uniformity of horizontal momentum provides an important moisture and energy-preserving mechanism for the generation and maintenance of the warm-core structure, and this mechanism in turn helps enhance the positive feedback process among moisture convergence, latent heat release and lower-level pressure falls that is responsible for the spinup of the mesovortex. It should be noted that the meso-α scale environmental wind in the vicinity of the vortex at this time shows weak anticyclonic flow with weak vertical shear of the horizontal wind up to 600 mb. Above and to the west of the vortex there is strong westerly shear. Such a vertical wind structure suggests that the nearly vertical temperature and vorticity perturbations associated with the mesovortex are more likely to persist below 500 mb than above due to the relatively weak ventilation effect (Lilly 1986).

As the rotating MCS decays and the diabatic heating decreases with time after 1200 UTC 7 July, the influence of the MCS on the environmental flow becomes less significant; this was also observed by McAnelly and Cotton (1986). This is especially true in the upper troposphere where the "blocking" effect rapidly diminishes as the mesoscale ascent weakens (see Figs. 14a, b). In particular, the relatively stronger wind shear in the upper troposphere tends to destroy the nearly vertically distributed mass perturbation associated with the vortex. Thus, some of the vorticity associated with the MCS at upper levels propagates downstream, and is gradually absorbed by the large-scale flow. On the other hand, within the low to midlevel environment, the relatively weak (actually negative) vertical wind shear, horizontal deformation, and stronger cyclonic vorticity suggest that the vortex-produced mass and moisture perturbations and the horizontal vortex circulation are more likely to be maintained by the inertial stability, as mentioned before. Furthermore, Fig. 14a shows that after 1800 UTC 7 July, the vorticity in the upper troposphere diminishes faster than that at midlevels; this is clearly due to the occurrence of a greater ventilation at upper levels. The reduction in vorticity at very low levels can be related to precipitation-driven subsidence (see Zhang et al. 1988).

Figures 20 and 21 compare the simulated 24-h upper-air structure valid at 0000 UTC 8 July to the corresponding observational analysis (see also the 1230 and 1631 UTC satellite images in Fig. 6). The capture of the mesoscale warm-core vortex by the standard upper-air observational network is rather unusual, especially considering that it was a closed cyclonic flow and there was such a long period after its genesis. In other cases, rotating MCSs tend to show up in the sounding data only as a weak cyclonic wind perturbation at one or two stations rather than four or five as in this case. Stull (1985) estimated the predictability of meso-β-scale circulations to be about 2–24 h. Although this 24-h simulation has reached the upper predictability limit, the model still demonstrates a capability for reproducing some important features. For example, the model was able to maintain the closed cyclonic wind circulation in lower levels (cf. Figs. 20c and 21d). Moreover, the simulated mesovortex occurs

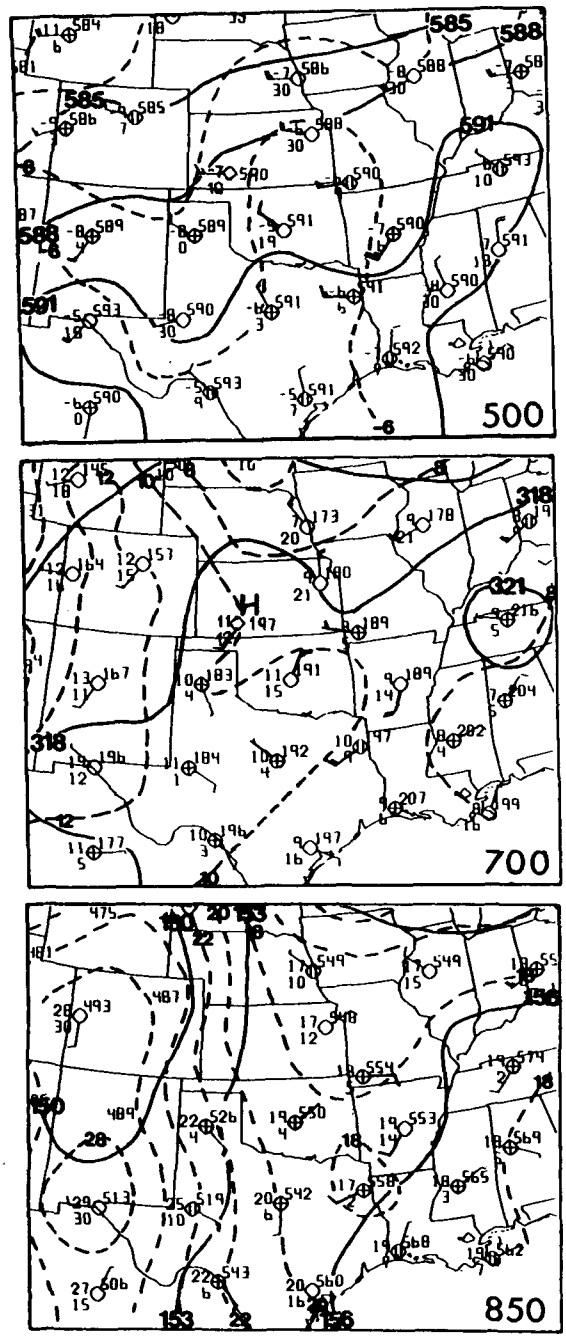

FIG. 20. As in Fig. 15a but for 0000 UTC 8 July 1982.

at approximately the right location. However, the vortex is somewhat smaller than the circulation appeared in the satellite imagery (cf. Figs. 6 and 21d). On the other hand, the horizontal deformation field is reproduced quite well. It is clear now that the vortex is located at the center of the horizontal deformation zone. The relatively weak environmental flow appears to be part of the reason that the MCS was able to generate a closed wind circulation since only a slight increase in pressure gradient could force the cross-isobaric component toward the vortex center. Note that the maximum vorticity is now located between 700 and 600 mb (cf. Figs. 14a, b) but the corresponding model wind circulation at those levels is not closed. In part II of this paper, such a high elevated vorticity maximum will be shown to be a consequence of the combined effects of the parameterized moist downdrafts, the resolvable-scale evaporative cooling, hydrostatic water loading and even the melting of ice.

In addition to the maintenance of the vortex, the model reproduces well the 700 mb meso-α-scale shortwave trough associated with the mesovortex, the approaching closed mesoanticyclone, and the wind perturbations and their magnitudes at 700 and 500 mb. Above 500 mb, both observations and the simulation shows rapid dissipation of vorticity perturbations, as discussed previously. It is interesting to note the vertical alignment of the vortex circulation center, i.e., it tilts toward the east (e.g., cf. Figs. 21b–d). This feature is more clearly apparent from vertical cross sections of relative vorticity, horizontal wind and equivalent potential temperature (see Fig. 22). The eastward tilting evidently is due to the presence of vertical wind shear. Specifically, the slow-moving, lower-level horizontal deformation field helps maintain the vortex as quasi-stationary (i.e., little eastward advection of vorticity) whereas the relatively large westerly wind component at upper levels tends to advect the circulation center downstream. The horizontal projection of this tilting up to 650 mb is about 75 km. Above this level, the vorticity center has been advected much farther downstream (see Fig. 22b). Although it is difficult to verify this numerical finding with the coarse-resolution observations, the vertical tilting of the vortex appears to have some important implications with respect to the vortex structure. For instance, the tilting of θ_e with height may help explain why in this or other case(s), a well-defined and persistent hydrostatically generated surface mesolow (such as shown in Rockwood et al. 1984; Zhang and Fritsch 1986a) was not evident either in the observations or the simulation. Instead, mesohighs and weak, transient low-pressure perturbations dominate the surface pressure distribution. Furthermore, since the air mass behind the front is cold and dry, its advection into the midtropospheric vortex layers due to the tilting tends to reduce the strength of the warm core temperature anomaly and prohibit the vertical penetration of strong upward motion. (Note the out-of-phase relationship between θ_e and upward motion above 650 mb in Fig. 22c.) The greatest amplitude of the warm-core structure has also now been shifted to roughly 800 mb (Fig. 22a) as the low-level cool pool subsides and gradually weakens. The appearence of low-level rotating stratiform clouds in the satellite im-

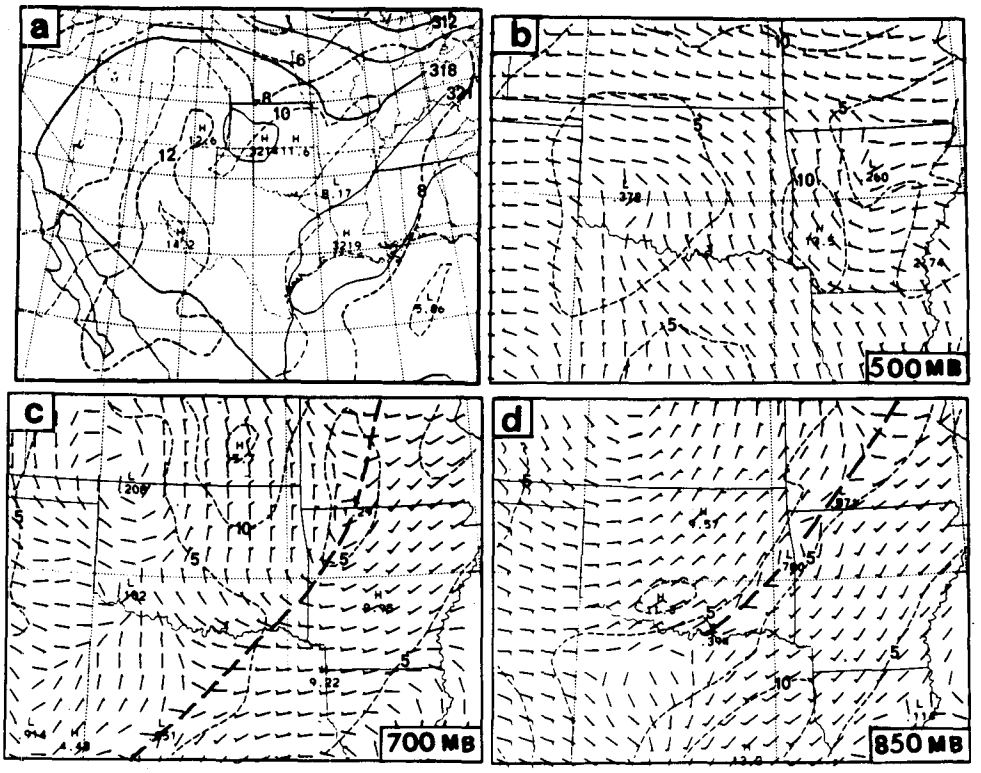

FIG. 21. Twenty four hour forecast of (a) 700 mb height (solid lines) and temperature (dashed lines); and (b)–(d) mesoscale wind field at every other point, valid at 0000 UTC 8 July 1982. Dashed lines denote isotach; a full barb is 10 m s^{-1}.

agery (Fig. 6) seems to support the above-discussed model results. Other simulated features to be noted from the cross section are the development of the well-mixed layer to the west of the vortex and the shallow, precipitation-produced cold, stable layer beneath and immediately to the east of the vortex (Fig. 22a). Also note the gravity wave-like distribution of mesoscale vertical motion (Fig. 22a).

Very surprisingly, by 36 h into the simulation (i.e., valid at 1200 UTC 8 July), the model still maintains the observed low-level closed cyclonic wind circulation at nearly the right place (cf. Figs. 23 and 24). Even more surprising is that the model deepened the layer exhibiting the closed wind circulation; namely, the closed circulation deepened from 800 mb to 600 mb in the 12-h period ending at the present time. In addition, the simulated amplification of the 700 mb shortwave trough and the scale of the vortex are comparable to observations. These model results are especially encouraging since the simulation of meso-β-scale weather systems up to 36 h is beyond traditional predictability concepts (see Anthes and Baumhefner 1984; Stull 1985). The long period of predictability of this mesovortex is probably due to the development of inertial stability and the presence of a weakly sheared environment. The former factor plays an important role in stiffening the dynamic and thermodynamic properties of the vortex. One may argue that the generation of a slight amount of the resolvable-scale condensation after 24 h might have helped the development of the deeper-layer closed circulation (see Fig. 7a). To support the significance of the inertial stability in maintaining the vortex circulation, an additional sensitivity experiment was performed in which all free atmospheric diabatic heating was gradually omitted within one model hour after 1800 UTC 7 July (i.e., 18 h into the simulation). The resulting 36-h simulation still shows the well-maintained closed wind circulation but with smaller values of cyclonic vorticity; this will be presented in part II of the paper. Nonetheless, it should be pointed out that the model did not produce everything correctly. For example, the simulation of the larger-scale environmental conditions degrades with time after 24 h. The model generates too extensive an area of the approaching mesoanticyclone and associated larger-scale ridge system in the midtroposphere. Because of this overprediction, the vortex center at 500 mb seems to have drifted a little too far to the south. Nevertheless, it appears that *the simulated mesovortex, once reasonably produced, would behave almost independently from*

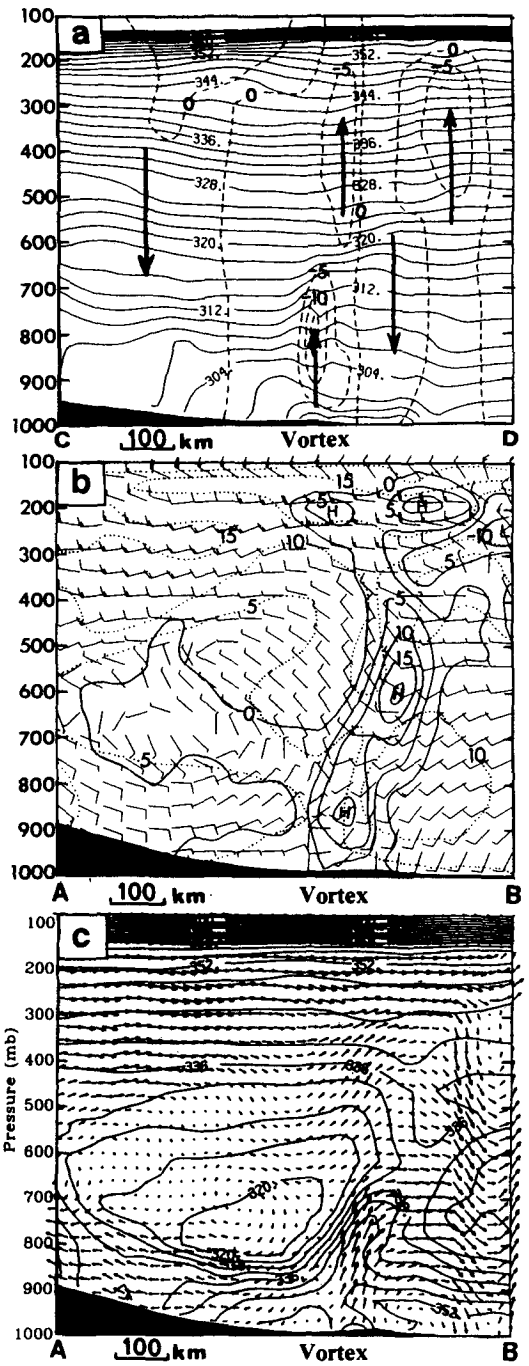

FIG. 22. (a) As in Fig. 19a but for 24-h forecast valid at 0000 UTC 8 July 1982. The cross section is taken along line CD in Fig. 12. (b) As in Fig. 19b but for 24-h forecast valid at 0000 UTC 8 July 1982. The cross section is taken along line AB in Fig. 12. (c) As in Fig. 19c but for 24-h forecast valid at 0000 UTC 8 July 1982. The cross section is taken along line AB in Fig. 12.

its simulated larger-scale environment unless the simulated environment departs very significantly from the natural evolution of events.

The vertical distribution of the simulated horizontal wind, vorticity, circulation vectors and θ_e (Fig. 25), along the same cross section as Figs. 22b and c, shows slight differences from that for the 24-h forecast. These differences include the occurrence of the closed wind circulation within a deeper layer, the penetration of organized upward motion ($\leq 10\ \mu b\ s^{-1}$) into the upper troposphere, less tilting of the vortex properties with

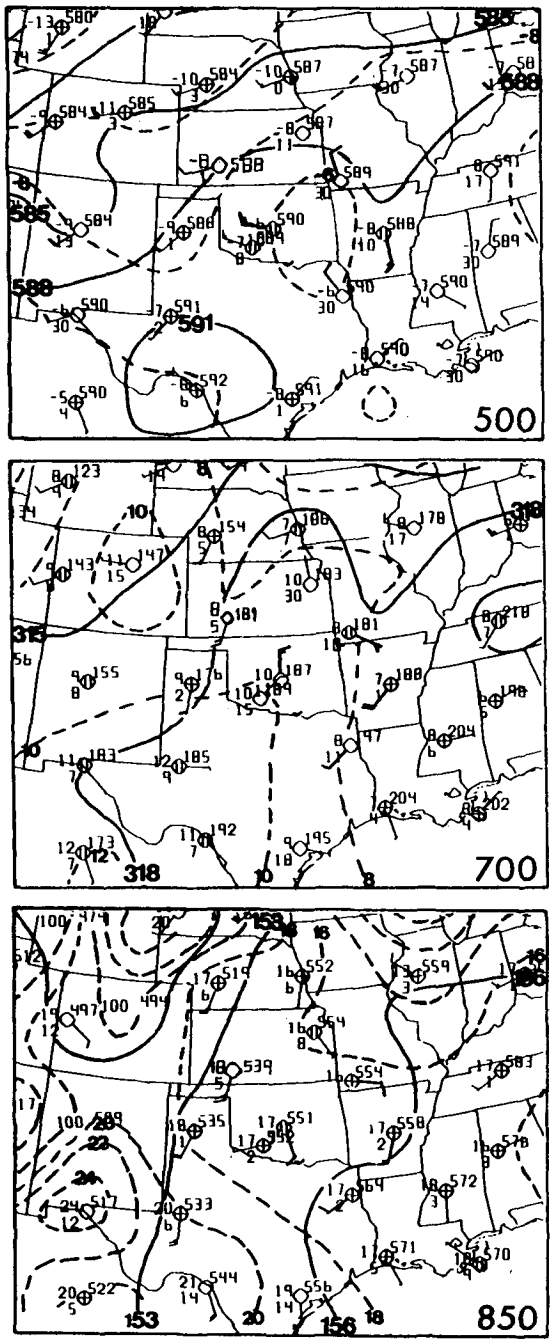

FIG. 23. As in Fig. 15a but for 1200 UTC 8 July 1982.

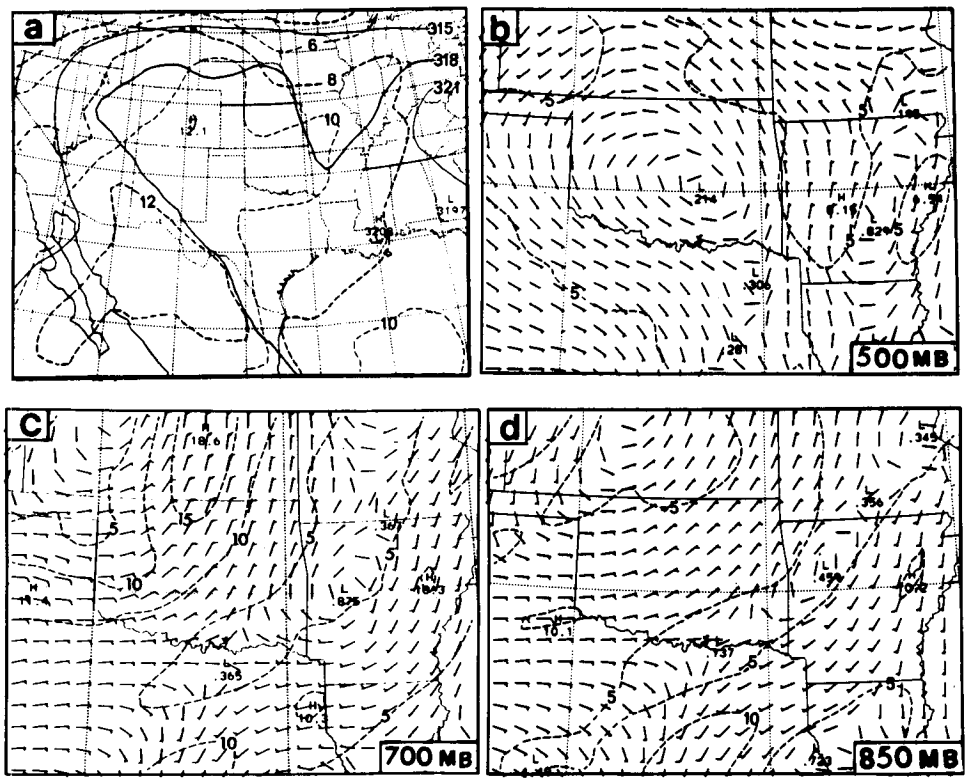

FIG. 24. As in Fig. 21 but for 36-h forecast valid at 1200 UTC 8 July 1982.

height, and the development of stronger anticyclonic flow below 600 mb to the west of the vortex. Note that the horizontal momentum is still uniformly distributed in the vertical and the vorticity maximum is located near 600 mb. The diagnostic calculation of the 1200 UTC 8 July vorticity profile by Menard et al. (1986) also shows the location of the vorticity maximum near 600 mb (see Fig. 14b). Again, these small differences can be attributed to the stiffening effect of inertial stability on the vortex properties and to the presence of a weakly sheared environment.

Finally, it is helpful to show the evolution of the model-generated 600 mb θ_e distribution for the understanding of the vortex development. A high-θ_e column near OKC at the initial time (see Figs. 26a and 5) appears to help define the location of the vortex generation through later release of latent heating. The mature vortex is characterized by a warm, moist core with θ_e values greater than 346 K in midtroposphere (Fig. 26b). Because of a sharp θ_e gradient associated with the vortex/front system, a stronger cyclonic circulation tends to entrain more high-θ_e air from the southwesterly flow ahead of the front, which is favorable for the intensification of the vortex. On the other hand, it tends to bring in more low-θ_e air from its rear to retard the development of the vortex (Figs. 26c and d). Thus, the strength of the vortex seems to be self-constrained. Sensitivity experiments, in which the vortices were simulated stronger than the control run during first 12 h due to the neglect of certain model physics, show that the vortex structures are similar to each other but have different magnitudes at the end of the 24-h simulation (not shown). The results appear to support the above-discussed self-constraint mechanism. It is interesting to note that the θ_e distribution associated with the vortex resembles quite well the midtropospheric moisture pattern suggested by the visible satellite imagery (i.e., cf. Figs. 26b, c and 6i, j).

5. Summary and concluding remarks

A 36-h numerical simulation of a meso-β-scale rotating MCS that occurred in Oklahoma during the period 0000 UTC 7 July–1200 UTC 8 July 1982 has been presented. A modified version of the PSU/NCAR mesoscale hydrostatic model was used to perform the simulation, and standard upper-air observations were utilized to initialize the model without any artificially constructed soundings. Although the simulated MCS formed a couple of hours later than the observed one, it evolved in a similar manner. Specifically, in the first

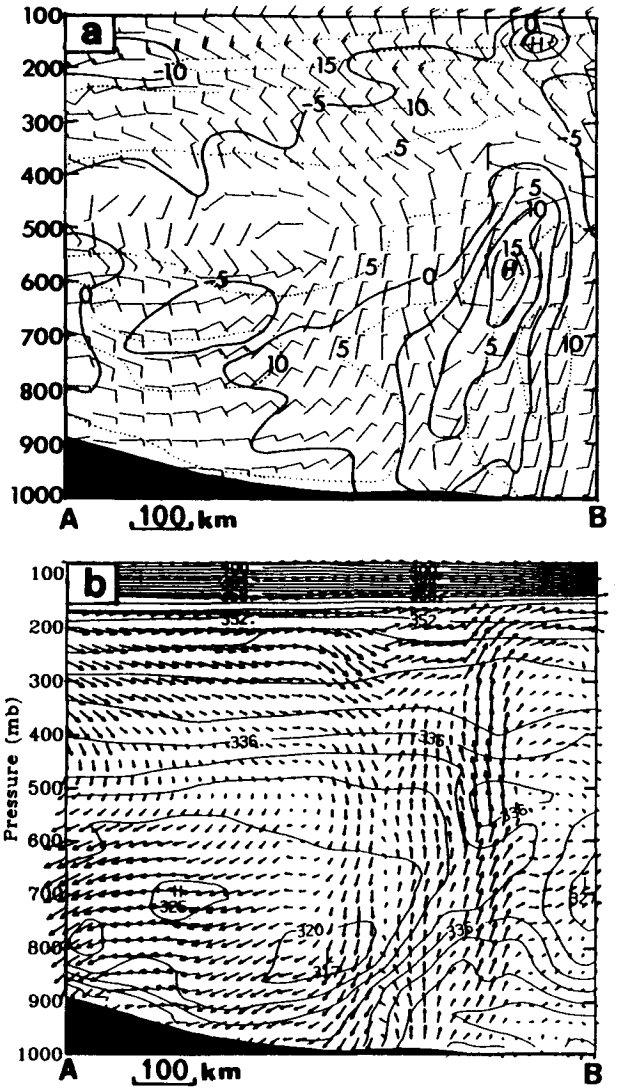

FIG. 25. (a) As in Fig. 19b but for 36-h forecast valid at 1200 UTC 8 July 1982. The cross section is taken along line AB in Fig. 12. (b) As in Fig. 19c but for 36-h forecast valid at 1200 UTC 8 July 1982. The cross section is taken along line AB in Fig. 12.

6 h into the simulation, a long line of deep convection developed along a surface front and then the convection consolidated as the rotating character began to appear. The model reproduces the observed genesis of the low- to midtropospheric closed wind circulation after 1200 UTC 7 July and the maintenance of the vortex structure thereafter. Likewise, the model simulates reasonably well the surface pressure perturbations, the evolution of moist convection, the magnitude and distribution of total rainfall, and other related surface features associated with the rotating MCS. In addition, the observed amplification of a midtropospheric shortwave trough, the development of an upper-level anticyclonic wind perturbation during the mature stage, the quasi-stationary nature of the vortex circulation, and the vertical distribution of horizontal momentum and relative vorticity in the vicinity of the vortex are all reasonably well simulated.

The mesovortex has a space scale of about 150–200 km in diameter. However, its influence on the environmental flow is on a much larger scale. The vertical structure of the vortex at its mature stage is characterized by low-level mesohigh pressure in association with a cool pool and sinking motion, a warm core structure in the midtroposphere with the strongest upward motion located between 400 and 300 mb, and an upper-level cold dome with an associated intense anticyclonic circulation. The cyclonic vorticity occurs within most of the troposphere with the maximum value near 700 mb. Horizontal momentum and equivalent potential temperature are uniformly distributed within the vortex layer, which is consistent with another vortex study by Zhang and Fritsch (1987). During the decaying stage, most of the vortex properties tilt downstream with height, and the vorticity maximum is shifted upward to near 600 mb. The low-level cool pool gradually weakens whereas the upper-level anticyclonic vorticity rapidly dissipates.

Both observed and simulated surface pressure disturbances show weak mesohighs beneath the vortex during the development stage and a relatively flat pressure distribution at later stages. Cross-sectional analysis of the model results reveals that the cool pools produced by evaporative cooling, melting, and parameterized moist downdrafts during the intenfying period and the tilting of the vortex circulation with height during the decaying period may explain why the surface pressure perturbations are so weak in this case. Verification of the surface features, particularly the surface pressure pattern, is considered to be very important for showing if the simulated rotating MCS has an intensity comparable to the observed, since it is well known that numerical models have little difficulty in spinning up vortices. In part II of this paper, it will be shown that without the above-mentioned model physics, the simulated mesovortex resembles a tropical cyclone with an intense mesoscale low pressure center beneath and a vortex circulation that extends over a much more extensive area than in the simulation presented in this paper.

Certain dynamic aspects of the development and evolution of the rotating MCS can be briefly summarized with the aid of Fig. 27 which shows the time evolution of the 850-mb analysis of stream lines, vertical motion and relative vorticity. In the initial period, note the anticyclonic southwesterly flow ahead of the front, and the anticyclonic northwesterly to northeasterly flow behind the front. The vorticity attains its maximum value along the frontal/pressure-trough axis due to the presence of the large wind shear (i.e., $\partial v/\partial x$). Note also that the vorticity is out of phase with

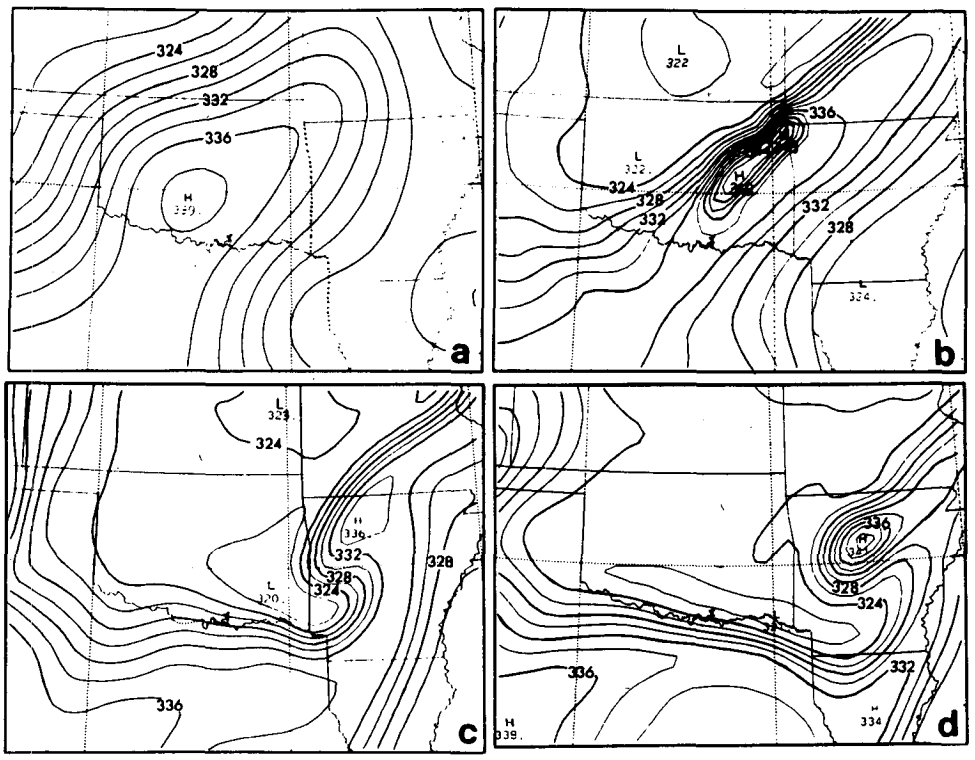

FIG. 26. Predicted evolution of 600 mb equivalent potential temperature at intervals of 2 K for (a) 0000 UTC 7 July 1982, (b) 1200 UTC 7 July 1982, (c) 0000 UTC 8 July 1982, and (d) 1200 UTC 8 July 1982.

the vertical motion and that there is cross frontal flow. The phase shift appears to be a propagation mechanism of the rotating MCS. The mechanism responsible for this phase shift is similar to that described by Orlanski and Ross (1984), and not likely associated with the gravity wave propagation described by Levy and Bretherton (1987), since the simulated convection ahead of the low-level front moves at a speed similar to the front.

Note that a vorticity center (denoted by the letter *C*), which appears to correspond to the initial 700 mb short wave over north-central Texas (Fig. 3), propagates northeastward along the front. Associated with it is the development of the local resolvable-scale rainfall maximum (not shown). The resolvable-scale condensation is primarily responsible for generating the vortex circulation through a positive feedback process among latent heat release, moisture convergence, low-level pressure falls and a wind adjustment process. In fact, the resolvable-scale condensation contributes 20% to 30% to the total rainfall. The rotating MCS decays as 1) the system moves into a thermodynamically stable regime; 2) low-θ_e air crosses the front from the rear and displaces the high-θ_e air ahead of the front; 3) the low-level, high-θ_e energy supply weakens; 4) deep convection to the south of the vortex intercepts the low-level supply of high-θ_e air; and 5) moist downdraft air lowers the equivalent potential temperature in the adjacent environment. It is found that the quasi-stationary nature of the mesovortex is related to the preexisting, quasi-stationary low-level horizontal deformation field. The vortex forms in the deformation field and tends to be long lived because of the weak low to midlevel shearing environment along the deformation axis. A relatively uniform distribution of horizontal momentum in combination with the generated large inertial stability also contribute to the longevity of the vortex.

In conclusion, the results suggest that for some cases, numerical forecasts of meso-β-scale characteristics, such as timing, location, structure and evolution, of rotating MCSs are feasible for time periods up to 36 h. Rotating MCSs appear to be more deterministic in terms of numerical prediction of their evolution than other types of MCSs to which the traditional predictability concepts are applied (see Anthes and Baumhefner 1984; Stull 1985). The successful generation of mesoscale features *from essentially large-scale initial conditions* is also one of the more significant aspects of the results. And finally, the results indicate that significant improvement in operational warm-season QPFs might be possible if additional experimental numerical simulations of the meso-β scale structure and evolution of MCSs are successful.

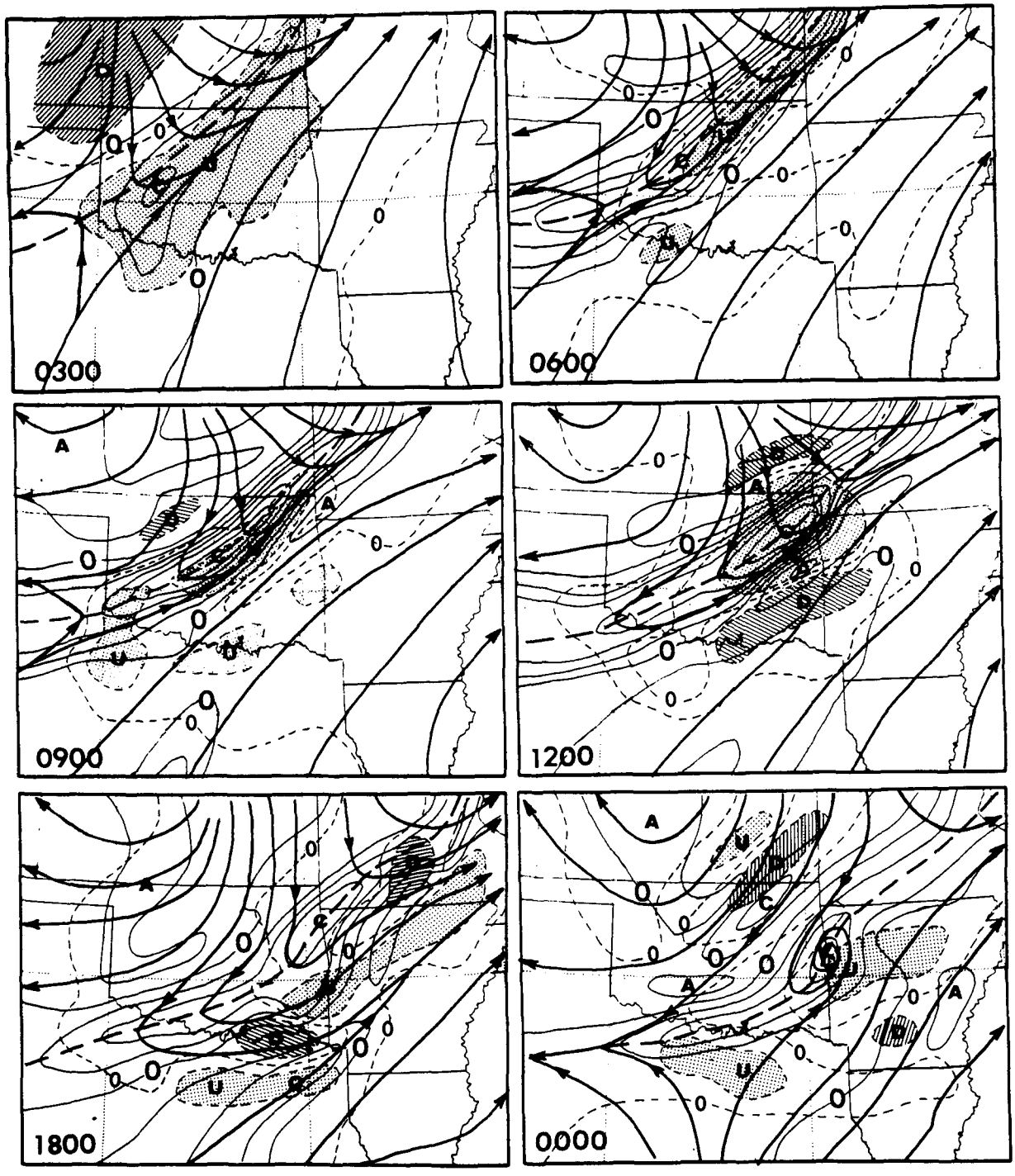

FIG. 27. Time evolution of streamlines (heavy solid lines), vertical motion (dashed lines, $\mu b\ s^{-1}$) and relative vorticity (thin solid lines at intervals of $5 \times 10^{-5}\ s^{-1}$) at 850 mb. The heavy dashed lines indicate the trough/frontal axis. Shading denotes an upward motion less than $-4\ \mu b\ s^{-1}$ and cross-hatching denotes a downward motion greater than $4\ \mu b\ s^{-1}$. The center of upward (downward) motion and cyclonic (anticyclonic) vorticity are represented by letters U (D) and C (A), respectively.

Acknowledgments. The National Science Foundation (NSF) is acknowleged for its support through Grant ATM-8711014, and the U.S. Air Force through Grant AFOSR-88-0050. We are grateful to Steven Rutledge, Ying-Hua Kuo and John Brown for their helpful reviewing comments. This work was initiated while the

first author (DLZ) was a research associate at the Pennsylvania State University and completed during DLZ's current tenure as an Advanced Study Programs Fellow at the Division of Mesoscale and Microscale Meteorology, National Center for Atmospheric Research which is sponsored by the National Science Foundation. We thank Mr. Menard for providing his mesoanalysis for the verification of the model simulation. The computation was performed on the NCAR CRAY X-MP.

REFERENCES

Anthes, R. A., and D. Keyser, 1979: Tests of a fine-mesh model over Europe and the United States. *Mon. Wea. Rev.*, **107**, 963–984.

——, and D. P. Baumhefner, 1984: A diagram depicting forecast skill and predictability. *Bull. Amer. Meteor. Soc.*, **65**, 701–703.

——, E.-Y. Hsie and Y.-H. Kuo, 1987: Description of the Penn State/NCAR mesoscale model version 4 (MM4.) 66pp. [Available from NCAR, TN-282, Boulder, CO 80307.]

Augustine, J. A., and K. W. Howard, 1987: The observed mesoscale kinematic and thermodynamic structure of an MCC at maturity. *Extended Abstracts, Third Conf. on Mesoscale Processes,* Amer. Meteor. Soc., p. 37.

Benjamin, S. G., and N. L. Seaman, 1985: A simple scheme for improved objective analysis in curved flow. *Mon. Wea. Rev.*, **113**, 1184–1198.

——, and T. N. Carlson, 1986: Some effects of surface heating and topography on the regional severe storm environment. Part I: Three dimensional simulation. *Mon. Wea. Rev.*, **114**, 307–329.

Bosart, L. R., and F. Sanders, 1981: The Johnstown flood of July 1977: A long-lived convective storm. *J. Atmos. Sci.*, **38**, 1616–1642.

Brandes, E. A., 1987: Kinematic and thermodynamic properties of the 6–7 May 1985 mesoscale convective system. *Extended Abstracts, Third Conf. on Mesoscale Processes,* Amer. Meteor. Soc., p. 109.

Carlson, T. N., S. G. Benjamin, G. S. Forbes and Y.-F. Li, 1983: Elevated mixed layers in the regional severe storm environment. *Mon. Wea. Rev.*, **111**, 1453–1473.

Chen, S.-J., and L. Dell'Osso, 1984: Numerical prediction of the heavy rainfall vortex over the eastern Asia Monsoon region. *J. Meteor. Soc. Japan*, **62**, 730–747.

Cho, H.-R., and D. S. Chan, 1987: Mesoscale atmospheric dynamics and modeling of rainfall fields. *J. Geophys. Res.*, **92**, 9687–9692.

Churchill, D. D., and R. A. Houze, Jr., 1984: Development and structure of winter monsoon cloud clusters on 10 December 1978. *J. Atmos. Sci.*, **41**, 933–960.

Fritsch, J. M., and C. F. Chappell, 1980: Numerical prediction of convectively driven mesoscale pressure systems. Part I: Convective parameterization. *J. Atmos. Sci.*, **37**, 1722–1733.

——, and R. A. Maddox, 1981: Convectively driven mesoscale pressure systems aloft. Part I: Observations. *J. Appl. Meteor.*, **20**, 9–19.

——, R. J. Kane and C. R. Chelius, 1986: The contribution of mesoscale convective weather systems to the warm-season precipitation in the United States. *J. Climate Appl. Meteor.*, **25**, 1333–1345.

Geogakakos, K. P., and M. D. Hudlow, 1984: Quantitative precipitation forecast techniques for use in hydrologic forecasting. *Bull. Amer. Meteor. Soc.*, **65**, 1186–1200.

Hack, J. J., and W. H. Schubert, 1986: Nonlinear response of atmospheric vortices to heating by organized cumulus convection. *J. Atmos. Sci.*, **43**, 1559–1573.

Heideman, K. F., and J. M. Fritsch, 1988: Forcing mechanisms and other characteristics of significant summertime precipitation. *Wea. Forecasting*, **3**(2), 115–130.

Hoskins, B. J., E. C. Neto and H.-R. Cho, 1984: The formation of multiple fronts. *Quart. J. Roy. Meteor. Soc.*, **110**, 881–896.

Houze, R. A., Jr., 1977: Structure and dynamics of a tropical squall-line system. *Mon. Wea. Rev.*, **105**, 1540–1567.

Hoxit, L. R., R. A. Maddox, C. F. Chappell, F. L. Zuckerberg, H. M. Mogil, I. Jones, D. R. Greene, R. E. Saffle and R. A. Scofield, 1978: Meteorological analysis of the Johnstown, Pennsylvania, flash flood, 19–20 July 1977. 71 pp. [Available from the U.S. Govt. Printing Office, Washington DC, 20402.]

Hsie, E.-Y., R. A. Anthes and D. Keyser, 1984: Numerical simulation of frontogenesis in a moist atmosphere. *J. Atmos. Sci.*, **41**, 2581–2594.

Johnson, R. H., 1986: The development of organized mesoscale circulations within Oklahoma–Kansas Pre-STORM convective systems. *Preprints, Inter. Conf. on Monsoon and Mesoscale Meteor.*, Taiwan, 100–104.

Johnston, E. C., 1981: Mesoscale vorticity centers induced by mesoscale convective complexes. M.S. thesis, Dept. of Meteorology, University of Wisconsin, 54 pp.

Kuo, Y.-H., L.-S. Cheng and R. A. Anthes, 1986: Mesoscale analysis of Sichuan flood catastrophe, 11–15 July 1981. *Mon. Wea. Rev.*, **114**, 1984–2003.

Leary, C. A., and E. N. Rappaport, 1987: The life cycle and internal structure of a mesoscale convective complex. *Mon. Wea. Rev.*, **115**, 1503–1527.

Levy, G., and C. S. Bretherton, 1987: On a theory of the evolution of surface cold fronts. *J. Atmos. Sci.*, **44**, 3413–3418.

Lilly, D. K., 1986: The structure, energetic and propagation of rotating convective storms. Part II: Helicity and storm stabilization. *J. Atmos. Sci.*, **43**, 126–140.

Lin, Y.-L., R. D. Farley and H. D. Orville, 1983: Bulk parameterization of the snow field in a cloud model. *J. Climate Appl. Meteor.*, **22**, 1065–1092.

McAnelly, R. L., and W. R. Cotton, 1986: Meso-β scale characteristics of an episode of meso-α-scale convective complexes. *Mon. Wea. Rev.*, **114**, 1740–1770.

Maddox, R. A., 1980: Mesoscale convective complexes. *Bull. Amer. Meteor. Soc.*, **61**, 1374–1387.

——, 1983: Large-scale meteorological conditions associated with midlatitude, mesoscale convective complexes. *Mon. Wea. Rev.*, **111**, 1475–1493.

——, D. J. Perkey and J. M. Fritsch, 1981: Evolution of upper tropospheric features during the development of mesoscale convective complex. *J. Atmos. Sci.*, **38**, 1664–1674.

Menard, R. D., 1988: Analysis of an MCC-generated inertially stable warm core vortex. M.S. thesis, Dept. of Meteorology, Pennsylvania State University, 79 pp.

——, J. H. Merritt, J. M. Fritsch and P. A. Hirschberg, 1986: Mesoanalysis of a convectively generated, inertially stable mesovortex. *Preprints, 11th Conf. on Weather Forecasting and Analysis,* Kansas City, Amer. Meteor. Soc., 194–199.

Molinari, J., and M. Dudek, 1986: Implicit versus explicit convective heating in numerical weather prediction models. *Mon. Wea. Rev.*, **114**, 1822–1831.

Ogura, Y., and M. T. Liou, 1980: The structure of a midlatitude squall line: A case study. *J. Atmos. Sci.*, **37**, 553–567.

Orlanski, I., and B. B. Ross, 1984: The evolution of an observed cold front. Part II: Mesoscale dynamics. *J. Atmos. Sci.*, **41**, 1669–1703.

Perkey, D. J., and C. W. Kreitzberg, 1976: A time-dependent lateral boundary scheme for limited-area primitive equation models. *Mon. Wea. Rev.*, **104**, 744-755.

——, and R. A. Maddox, 1985: A numerical investigation of a mesoscale convective system. *Mon. Wea. Rev.*, **113**, 553–566.

Ramage, C. S., 1982: Have precipitation forecasts improved? *Bull. Amer. Meteor. Soc.*, **63**, 739–743.

Rockwood, A. A., D. L. Bartels and R. A. Maddox, 1984: Precipitation characteristics of a dual mesoscale convective complex. NOAA Tech. Rep. ERL ESG-6, 50 pp. [Available from NOAA, Boulder, CO 80302.]

Ross, B. B., and I. Orlanski, 1982: The evolution of an observed cold front. Part I: Numerical simulation. *J. Atmos. Sci.*, **39**, 296–327.

Rutledge, S. A., and P. V. Hobbs, 1983: The mesoscale and microscale structure and organization of clouds and precipitation in midlatitude cyclones. Part VIII: A model for the "seeder–feeder" process in warm-frontal rainbands. *J. Atmos. Sci.*, **40**, 1185–1206.

Schubert, W. H., and J. J. Hack, 1982: Inertial stability and tropical cyclone development. *J. Atmos. Sci.*, **39**, 1687–1697.

Smith, R. K., 1981: The cyclostrophic adjustment of vortices with application to tropical cyclone modification. *J. Atmos. Sci.*, **38**, 2021–2030.

Smull, B. F., and R. A. Houze, Jr., 1985: A midlatitude squall line with a trailing region of stratiform rain: Radar and satellite observations. *Mon. Wea. Rev.*, **113**, 117–133.

——, and ——, 1987: Dual-Doppler radar analysis of a midlatitude squall line with a trailing region of stratiform rain. *J. Atmos. Sci.*, **44**, 2128–2148.

Stull, R. B., 1985: Predictability and scales of motion. *Bull. Amer. Meteor. Soc.*, **66**, 432–436.

Velasco, I., and J. M. Fritsch, 1987: Mesoscale convective complexes in the Americas. *J. Geophys. Res.*, **92**, 9591–9613.

Wang, B., and I. Orlanski, 1987: Study of a heavy rain vortex formed over the eastern flank of the Tibetan plateau. *Mon. Wea. Rev.*, **115**, 1370–1393.

Wetzel, P. J., W. R. Cotton and R. L. McAnelly, 1983: A long-lived mesoscale convective complex. Part II: Evolution and structure of the mature complex. *Mon. Wea. Rev.*, **111**, 1919–1937.

Wu, G.-X., and S.-J. Chen, 1985: The effect of mechanical forcing on the formation of a mesoscale vortex. *Quart. J. Roy. Meteor. Soc.*, **111**, 1049–1070.

Zhang, D.-L., 1989: The effect of parameterized ice microphysics on the simulation of vortex circulation with a mesoscale hydrostatic model. *Tellus*, **41A**, in press.

——, and R. A. Anthes, 1982: A high-resolution model of the planetary boundary layer—sensitivity tests and comparisions with SESAME-79 data. *J. Appl. Meteor.*, **21**, 1594–1609.

——, and J. M. Fritsch, 1986a: Numerical simulation of the meso-β scale structure and evolution of the 1977 Johnstown flood. Part I: Model description and verification. *J. Atmos. Sci.*, **43**, 1913–1943.

——, and ——, 1986b: A case study of the sensitivity of the numerical simulation of mesoscale convective systems to varying initial conditions. *Mon. Wea. Rev.*, **114**, 2418–2431.

——, and ——, 1987: Numerical simulation of the meso-β scale structure and evolution of the 1977 Johnstown flood. Part II: Inertially stable warm-core vortex and the mesoscale convective complex. *J. Atmos. Sci.*, **44**, 2593–2612.

——, and ——, 1988: Numerical sensitivity experiments of varying model physics on the structure, evolution and dynamics of two mesoscale convective systems. *J. Atmos. Sci.*, **45**, 261–293.

——, H.-R. Chang, N. L. Seaman, T. T. Warner and J. M. Fritsch, 1986: A two-way interactive nesting procedure with variable terrain resolution. *Mon. Wea. Rev.*, **114**, 1330–1339.

——, E.-Y. Hsie and M. W. Moncrieff, 1988: A comparision of explicit and implicit predictions of convective and stratiform precipitating weather systems with a meso-β scale numerical model. *Quart. J. Roy. Meteor. Soc.*, **114**, 31–60.